



TECHNISCHE UNIVERSITÄT WIEN

MASTER THESIS

---

Out-of-plane excitation of MEMS resonators in  
the MHz range with a planar electrostatic  
transducer arrangement

---

*Author:*  
Michael Gully

*Supervisor:*  
Prof. Dr. Ulrich Schmid

*Co-Supervisor:*  
Dr. Georg Pfusterschmied  
Dominik Huber, MSc

April, 2024



## Acknowledgments

First of all, I would like to thank Prof. Dipl.-Phys. Dr.rer.nat. Ulrich Schmid, who gave me the opportunity to carry out this work.

My next thanks goes to Univ.Ass. Dipl.-Ing. Dr.techn. Georg Pfusterschmied. Through constructive discussions and his feedback, this work became what it is.

Special thanks are due to my supervisor Dipl.-Ing. Dominik Huber, whose technical expertise, patience and tireless support have made a decisive contribution to the successful completion of this thesis.

I would also like to thank my fellow students Christoph and Patricia, who created a positive working environment and were always willing to discuss and share ideas.

Further thanks go to my long-time friends David and Patrick, who have accompanied and encouraged me throughout my studies.

Finally, I would like to thank my parents Gerlinde and Peter, and my brother Johannes for their unconditional support.



Die approbierte gedruckte Originalversion dieser Diplomarbeit ist an der TU Wien Bibliothek verfügbar  
The approved original version of this thesis is available in print at TU Wien Bibliothek.

## Kurzfassung

MEMS (micro electro-mechanical systems) Resonatoren in einen definierten, mechanischen Schwingungszustand anzuregen kann auf unterschiedliche Arten erfolgen. In dieser Arbeit wird ein Konzept für die elektro-statische Anregung von out-of plane Moden präsentiert, wobei sich beide Elektroden des Transducerelementes in einer Ebene befinden. Die Fabrikationsschritte für diesen Transducer sind auf ein Minimum reduziert, um eine einfache Herstellung zu ermöglichen. Als Material für die Resonatoren kommen wenige Mikrometer dünne Schichten aus polykristallinem Silizium und polykristallinem Diamant zum Einsatz. Die Anregemöglichkeit von unterschiedlichen Moden wird mit verschiedenen Elektrodenkonfigurationen getestet und verglichen. Als Resonatorgeometrie kommen sowohl lange, schmale Balken als auch breiten Plattenresonatoren zum Einsatz. Des Weiteren erfolgt ein Vergleich dieser Anregungsmethode mit einer thermo-mechanischen Anregung, die kontaktlos mit einem Laser erfolgt. Neben der Charakterisierung von materialspezifischen Eigenschaften von MEMS Resonatoren wird darüber hinaus die potentielle Anwendung dieses Transducers im Prozessmonitoring auf Waferebene während der Herstellung von MEMS diskutiert.

## Summary

MEMS (micro electro-mechanical systems) resonators can be excited into a defined mechanical oscillation state in different ways. In this work, a concept for the electrostatic actuation of out-of-plane modes is presented, where both electrodes of the transducer element are located in one plane. The fabrication steps for this transducer are reduced to a minimum in order to enable a simplified production. The material used for the resonators are thin layers of polycrystalline silicon and polycrystalline diamond just a few micrometers thin. The excitation possibilities of different modes are tested and compared with different electrode configurations. Both long, narrow bars and wide plate resonators are used as the resonator geometry. Furthermore, this excitation method is compared with thermo-mechanical actuation, which is carried out contactlessly with a laser. In addition to the characterization of material-specific properties of MEMS resonators, the potential application of this transducer in process monitoring at wafer level during the manufacture of MEMS is also discussed.



# Contents

<b>1</b>	<b>Introduction</b>	<b>1</b>
<b>2</b>	<b>Theory</b>	<b>3</b>
2.1	Mechanical Beam and Plate Resonators . . . . .	3
2.1.1	Euler-Bernoulli Approximation for Long Beams . . . . .	3
2.1.2	Mode Shape Analysis for Plate Resonators . . . . .	4
2.1.3	Damping . . . . .	6
2.1.4	Controllability and Observability . . . . .	8
2.2	Actuation mechanisms for MEMS . . . . .	10
2.2.1	Thermal Actuation . . . . .	10
2.2.2	Electromagnetic Actuation . . . . .	11
2.2.3	Piezoelectric Actuation . . . . .	11
2.2.4	Electrostatic Actuation . . . . .	12
2.3	Concept for Electrostatic Actuation . . . . .	14
<b>3</b>	<b>Transducer Principle and Experimental Details</b>	<b>17</b>
3.1	Placement of the Electrodes . . . . .	17
3.1.1	Single Electrode . . . . .	17
3.1.2	Dual Electrode . . . . .	18
3.1.3	Layer Thickness Variation . . . . .	18
3.2	Description of the Measuring Equipment . . . . .	19
3.2.1	Scanning Electron Microscope . . . . .	19
3.2.2	Profilometer . . . . .	19
3.2.3	Laser-Doppler Vibrometer . . . . .	20
3.2.4	Lock-In Amplifier . . . . .	20
3.2.5	Laserdriver . . . . .	21
3.3	Device Layer Materials . . . . .	22
3.4	Fabrication Parameters and Settings . . . . .	24
3.4.1	Technologies . . . . .	24
3.4.2	Fabrication Steps for Undoped Materials . . . . .	28
3.4.3	Fabrication Steps for Doped Materials . . . . .	29
3.4.4	Fabricated Devices . . . . .	32
3.5	Measurement Setup for Resonances . . . . .	33
3.5.1	Photo-Thermal Actuation . . . . .	34
3.5.2	Electrostatic Actuation . . . . .	34
3.6	Measurement Procedure . . . . .	35
3.6.1	Electrical Contacting inside the Vacuum Chamber . . . . .	35
3.6.2	Detecting Resonant Frequencies . . . . .	35

3.6.3	Resonance Fit . . . . .	40
3.6.4	Mode Identification . . . . .	41
3.7	Circular Transmission Line Measurement . . . . .	42
3.8	Layer Thickness Measurement . . . . .	43
<b>4</b>	<b>Results and Proof of Concept</b>	<b>45</b>
4.1	Linearity of the Electrostatic Actuation . . . . .	45
4.2	Bandwidth Limitation . . . . .	46
4.3	Euler–Bernoulli Beams . . . . .	47
4.3.1	Single Electrode Design . . . . .	47
4.3.2	Dual Electrode Design . . . . .	49
4.4	Plate Resonators . . . . .	54
<b>5</b>	<b>Conclusions and outlook</b>	<b>57</b>
	<b>List of Figures</b>	<b>64</b>

# 1 Introduction

The field of electrical engineering has been greatly impacted by micro-electro-mechanical systems (MEMS), which enabled the creation of compact sensors and actuators with microscale dimensions. A first demonstration of such a micro machined system in the year 1967 was an underetched metal cantilever employed in a resonant gate transistor [1]. In the following decades, more and more micro mechanical components such as springs, hinges, gears and so on were fabricated in laboratories [2]. A little later, the first commercial products appeared on the market, including acceleration sensors for the deployment of car airbags [3]. Today, many miniaturized sensors and actuators are manufactured using processes from semiconductor production. Smartphones and wearables such as smartwatches in particular rely heavily on MEMS technology, as the high degree of miniaturization would hardly have been possible with conventional precision engineering methods.

In order to be able to measure non-electrical properties, such as movement in space, temperature and time, mechanical resonators play an important role for MEMS. Examples are gyroscopes to measure spatial translation [4], sensors for detecting chemicals or to determine the viscosity of liquids [5]. Another example are MEMS-based timing devices, which can keep up with the performance of established quartz oscillators, and are also becoming an increasingly important consumer branch [6]. For this type of devices, a suitable choice of vibration actuation to maintain a continuous oscillation is important, which can be achieved by utilising various physical effects. The typical actuator principles for MEMS are based on thermal, magnetic, piezoelectric and electrostatic effects. The disadvantage of both thermal and magnetic actuators is that they have a high power consumption due to joule losses. With piezoelectric actuation, an additional piezoelectric layer must be placed on the resonator, which changes the properties of the resonator and also therefore also requires more fabrication steps. This work utilizes the principle of electrostatic actuation, which requires only two electrically conductive plates, making it not only simple but also easy to fabricate.

To actuate the out-of-plane modes of cantilevers and plate resonators, a simple to fabricate electrode design is developed. The operational capability of this transducer design is evaluated on different resonators made of polycrystalline materials.



### 2.1 Mechanical Beam and Plate Resonators

#### 2.1.1 Euler-Bernoulli Approximation for Long Beams

Beams where the length is much larger than the width and thickness are referred to as Euler-Bernoulli beams. A simplified, two-dimensional analysis can be carried out for such beams.

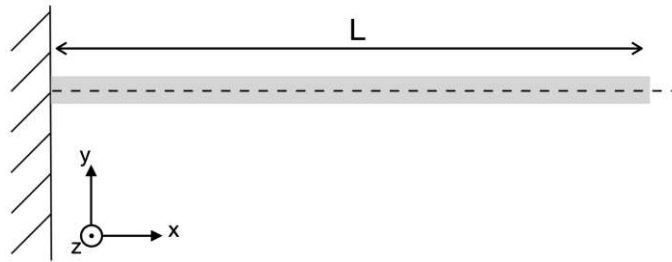


**Figure 2.1:** Two dimensional model of a single side clamped cantilever, also called *Euler-Bernoulli beam*.

Given the beam in Figure 2.1 and neglecting damping, a vibrating oscillation of the cantilever beam must satisfy

$$EI \frac{\partial^4 y(x, t)}{\partial x^4} = \rho \frac{\partial^2 y(x, t)}{\partial t^2}, \quad (2.1)$$

where  $E$  is Young's modulus,  $I$  is the cross-sectional moment of inertia around the  $z$ -axis and  $\rho$  is the mass density. Equation (2.1) can be separated into a spatial and a temporal part using separation of variables (Equation (2.2)) for the deflection  $y(x, t)$ .

$$y(x, t) = Y(x)C(t) = Y(x)C_0 \cos(\omega_r t - \phi) \quad (2.2)$$

Inserting the ansatz from Equation (2.2) into Equation (2.1) leads to

$$\frac{d^4 Y(x)}{dx^4} = \beta^4 Y(x) \quad \text{where} \quad \beta^4 = \frac{\rho \omega_r^2}{EI}. \quad (2.3)$$

To solve this differential equation, it is necessary to define the boundary conditions for the fixed part of the beam and the free end

$$\begin{aligned} Y(x) = 0 \quad , \quad \frac{dY(x)}{dx} = 0 \quad & \text{at} \quad x = 0 \\ EI \frac{d^2 Y(x)}{dx^2} = 0 \quad , \quad -EI \frac{d^4 Y(x)}{dx^4} = 0 \quad & \text{at} \quad x = L. \end{aligned} \quad (2.4)$$

This differential equation has an infinite number of solutions, with each solution  $Y_n(x)$  (called *mode shape* or simply *mode*) having an associated resonant frequency  $\omega_n$

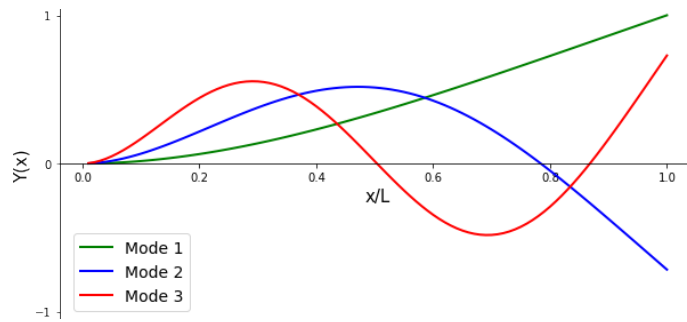


**Figure 2.2:** First three mode shapes of the simple Euler-Bernoulli cantilever

$$Y_n(x) = A \left[ \sin \beta_n x - \sinh(\beta_n x) - \frac{\sin(\beta_n L) + \sinh(\beta_n L)}{\cos(\beta_n x) + \cosh(\beta_n L)} (\cos(\beta_n x) - \cosh(\beta_n x)) \right] \quad (2.5)$$

$$\omega_n = s_n^2 \sqrt{\frac{EI}{\rho L^4}} \quad \text{where} \quad s_n^2 = \beta_n L \quad \text{which satisfies} \quad \cos(\beta L) \cosh(\beta L) = -1.$$

Notably, the resonant frequencies depend on the material parameters, but the mode shapes only depend on the geometry of the beam. Consequently, two geometrically identical cantilevers made of different materials have the same mode shape but at different resonant frequencies.

The first three mode shapes of the cantilever are shown in Figure 2.2. Points at which the beam undergoes no deflection are called *nodes* or *nodal lines*. The first mode has only one node at the fixed side, the second mode, on the other hand, has another node after approx. 80% of the length of the cantilever. This pattern continues, as each additional mode always has one more node than the previous one. The maximum deflection for each mode shape is always found at the free end of the cantilever.

### 2.1.2 Mode Shape Analysis for Plate Resonators

In the three-dimensional case, nodal lines are formed across the resonator. Some examples of narrow, long cantilever and wide plate resonators are shown in Figure 2.3 and Figure 2.4. The numbering of the modes is based on counting the nodal lines along the width and length of the cantilever as shown in Figure 2.5. In comparison with the two-dimensional analysis of a cantilever, modes with nodal lines along the length of the beam are now also possible in the three-dimensional model. For both resonator shapes, the largest deflection for each mode occurs at the free-swinging corners.

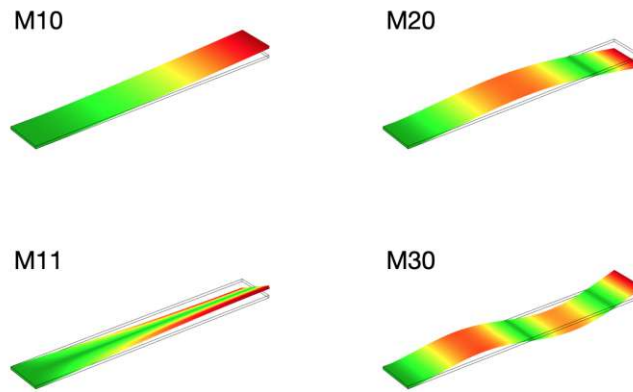


**Figure 2.3:** The first four mode shapes of a thin single-side clamped cantilever with a length to width ratio of 20:3. The color gradient shows the deflection, with green indicating no deflection and red the largest deflection.

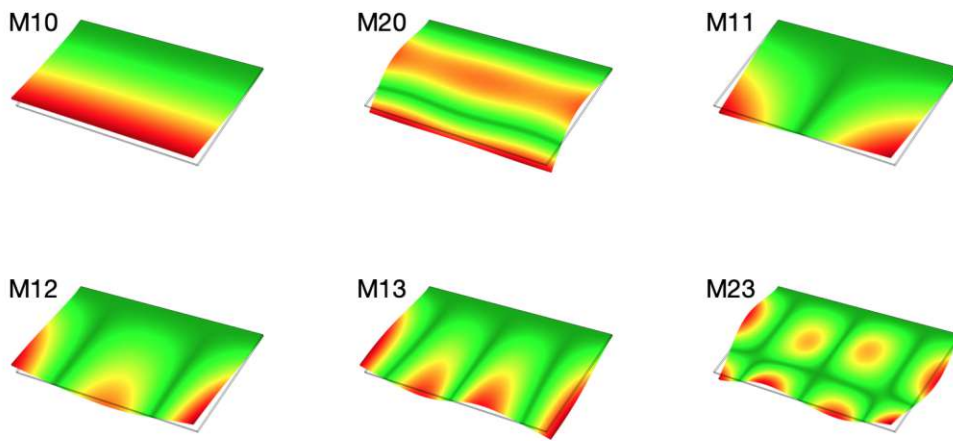


**Figure 2.4:** A few examples of mode shapes of a thin plate clamped on one side with a length to width ratio of 1:2.

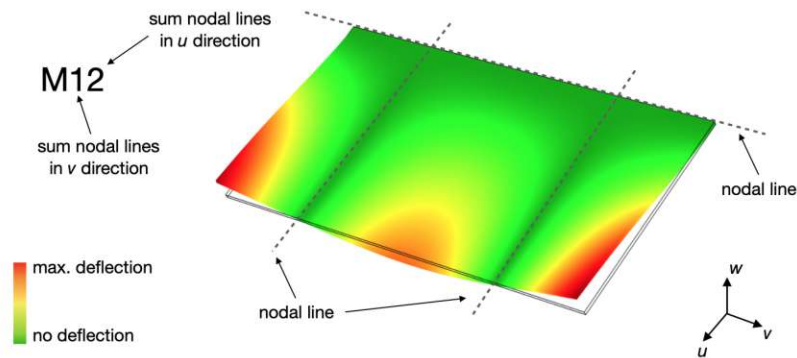


**Figure 2.5:** The mode shapes are labeled by enumerating the nodal lines as illustrated

### 2.1.3 Damping

In contrast to the previous models, real systems typically exhibit dampening, which dissipates a portion of the energy.

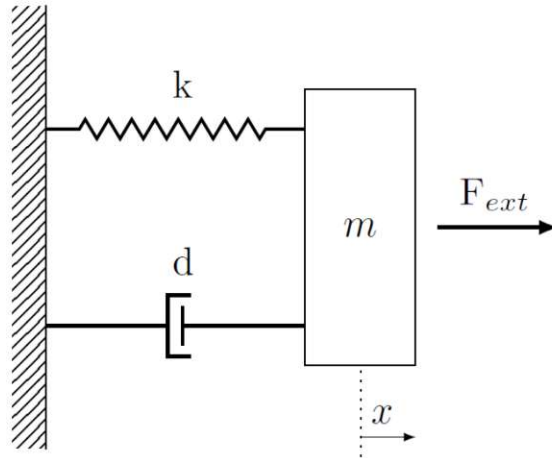


**Figure 2.6:** Mechanical model of a damped harmonic oscillator with external excitation. The mass  $m$  is connected to a spring  $k$  and a damper  $d$  on a rigid surface, with an external force  $F_{ext}$  acting on the mass.

A simple example of a harmonic mechanical oscillator is shown in fig. 2.6. The mass  $m$ , which is being connected to a rigid surface via a spring  $k$  and a damper  $d$ , can only move in the  $x$ -direction. In addition, an external force ( $F_{ext}$ ) acts on the mass. The differential Equation

$$F_{ext} = m\ddot{x} + d\dot{x} + kx, \quad (2.6)$$

can be derived for this system, which after transformation into the Laplace domain

$$\hat{F}_{ext} = ms^2\hat{x} + ds\hat{x} + k\hat{x}, \quad (2.7)$$

describes the behavior of the system in the form of the transfer function

$$G(s) = \frac{\hat{x}}{\hat{F}_{ext}} = \frac{\frac{1}{k}}{\frac{s^2}{\omega_0^2} + 2\zeta\frac{s}{\omega_0} + 1} \quad \text{where} \quad \omega_0 = \sqrt{\frac{k}{m}} \quad \text{and} \quad \zeta = \frac{d}{2\sqrt{mk}}. \quad (2.8)$$

The magnitude and phase for different values of  $\zeta$  are shown in Figure 2.7. The peak amplitude increases for smaller damping and increases to infinity for no damping (this is referred to as the resonance disaster). If the damping gets to high ( $\zeta \leq \sqrt{2}$ ), the system no longer exhibits a resonance boost. The position of the resonance peak is precisely at  $\omega_0$  only for an undamped system, the higher the damping, the further the maximum deflection shifts towards low frequencies. However, the point at which the phase has reached  $-90^\circ$  is, independent of damping, at exactly  $\omega_0$ . Due to damping, part of the

energy dissipates, which means that the amplitude of the system, without an external force, decreases with each period. The quotient of the stored energy to the dissipated energy over a period is referred to as the quality factor or  $Q$ -factor and can be expressed as

$$Q = 2\pi \frac{\text{energy stored}}{\text{energy dissipated per cycle}} = \frac{1}{2\zeta}. \quad (2.9)$$

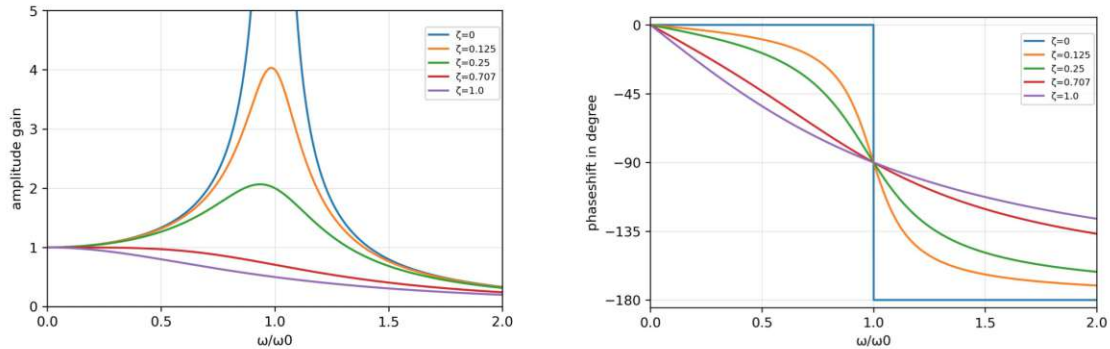


**Figure 2.7:** Amplitude gain and phase of the harmonic oscillator with different values for  $\zeta$ .

For a resonator in a vacuum, there are several loss mechanisms [7] which together form the total  $Q$ -factor

$$\frac{1}{Q} = \frac{1}{Q_{clamping}} + \frac{1}{Q_{TED}} + \frac{1}{Q_{volume}} + \frac{1}{Q_{surface}} + \dots \quad (2.10)$$

Among other mechanisms, energy is dissipated in the anchor of the resonator ( $Q_{clamping}$ ), through thermoelastic damping ( $Q_{TED}$ ), volumetric ( $Q_{volume}$ ) and on the surface ( $Q_{surface}$ ).

As an example, Figure 2.8 shows the amplitude and phase response of the first three modes of some arbitrary resonator. The combined response of a resonator is the sum of all the individual resonances (Figure 2.9).

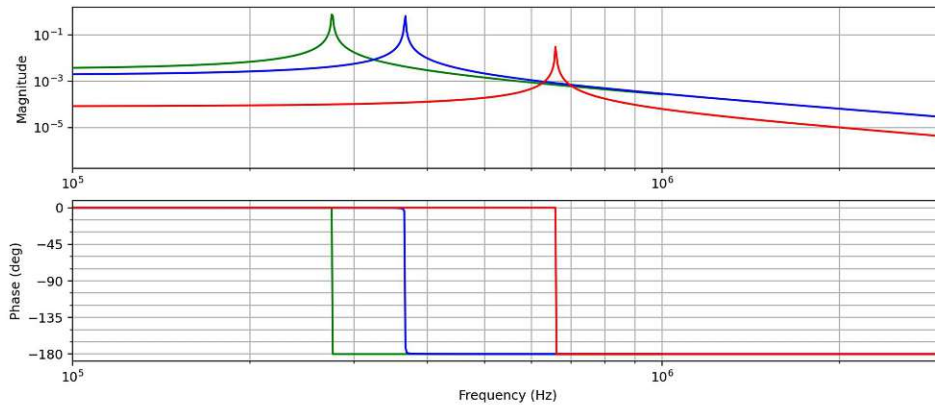


**Figure 2.8:** Bode plot of the first three resonances of an arbitrary resonator

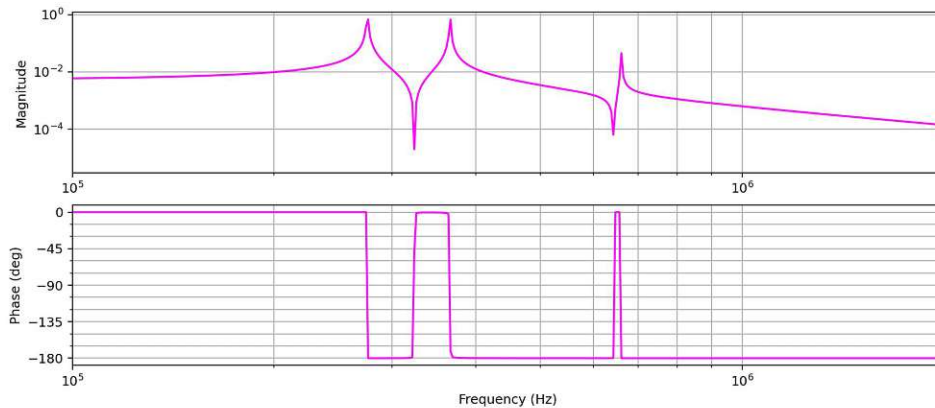


**Figure 2.9:** Bode plot of the sum of the first three resonances of an arbitrary resonator as depicted in Figure 2.8

### 2.1.4 Controllability and Observability

In order to actuate the different mode shapes of a resonator an external, periodic force is required. Through the illustration of a damped two-dimensional cantilever, the influence of force placement on resonance amplitudes is showcased in different scenarios (Figure 2.10). When the external force acts at point  $\alpha$ , only the first out-of-plane mode can be actuated, as the actuation point coincides with the node of the second out-of-plane mode. The point  $\beta$ , on the other hand, represents a point of maximum amplitude for both mode shapes, therefore both modes will be actuated. If a comparison is made between the effect of the different location of forces on first out-of-plane mode, point  $\beta$  will produce a larger deflection than a force of the same magnitude at point  $\alpha$ . In order to be able to actuate all modes, the force must not be located at a node. The largest amplitude will occur, when the force acts on a point of maximum deflection for each mode shape.

In order to be able to detect the modes, the measuring has to be at a place on the cantilever that does not have a nodal spot on the respective mode shape. If  $\alpha$  is selected as the measuring point and the external force acts on  $\beta$ , both modes are actuated, but the deflection of the second out-of-plane mode is not observable. The best possible measuring point is therefore again the point with the largest deflection for all modes.

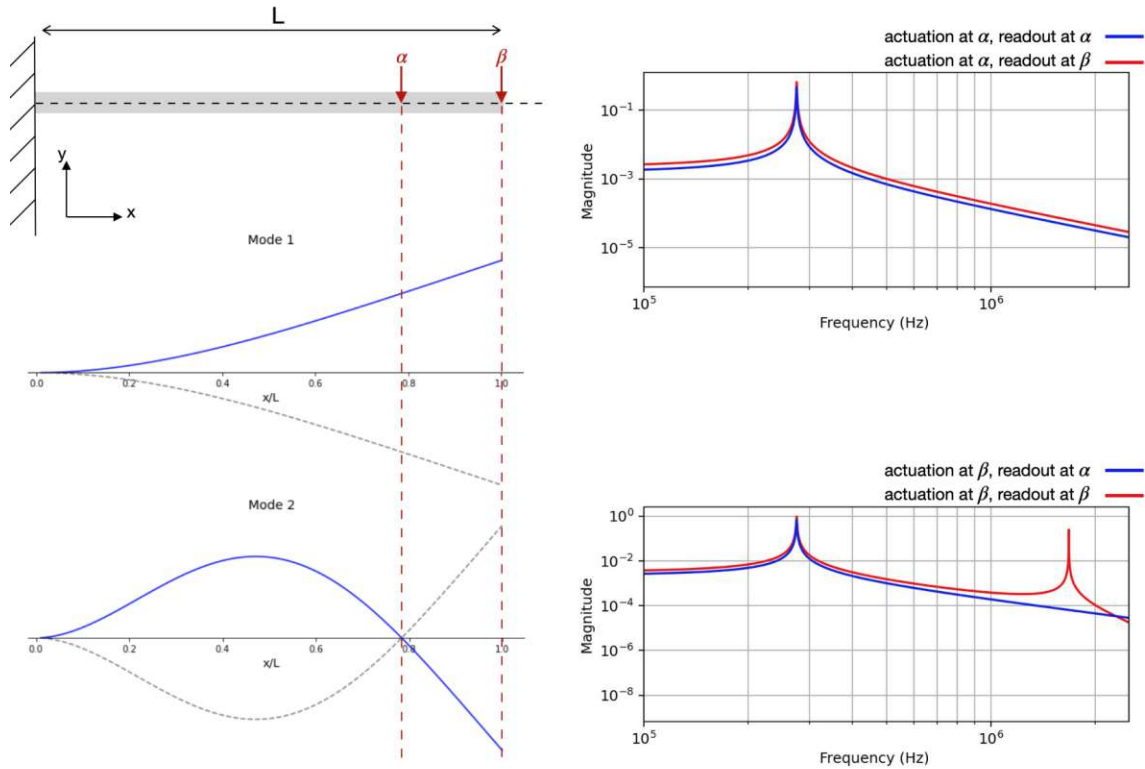


**Figure 2.10:** Deflection of various points on a cantilever: Point  $\alpha$  is located on the node of the second mode, at  $\beta$  the maximum deflection occurs for both mode shapes. The amplitude responses on the right-hand side show the deflection of the beam measured at the different actuation and measurement points.

## 2.2 Actuation mechanisms for MEMS

The most commonly used mechanisms for actuation in micromechanical applications are thermal, electromagnetic, piezoelectric and electrostatic [8].

### 2.2.1 Thermal Actuation

The expansion of a material with varying temperature can be expressed using

$$\Delta l = l_0 \kappa \Delta T, \quad (2.11)$$

where  $\Delta l$  is the elongation change,  $l_0$  the initial length,  $\kappa$  the coefficient of thermal expansion and  $\Delta T$  the temperature change. Such a temperature change can be achieved by applying a current to an electrically conductive element, the Joule losses in the material cause the latter to heat up and thus expand (Figure 2.11 a). Another method is to place a heating element between two materials with different expansion coefficients, the difference in stress causes the structure to bend (Figure 2.11 b). However, thermal energy can also be applied to a material without making any contact using for example a laser. In this case, a cantilever is heated with a laser and the resulting stress on that side leads to deformation (Figure 2.11 c). The major advantages of thermal excitation are the relatively large deflections and the large forces that can be achieved. The disadvantages include the high energy requirement and the high currents. The achievable frequencies are strongly dependent on the material, as the material has to dissipate the thermal energy to return to its original position.

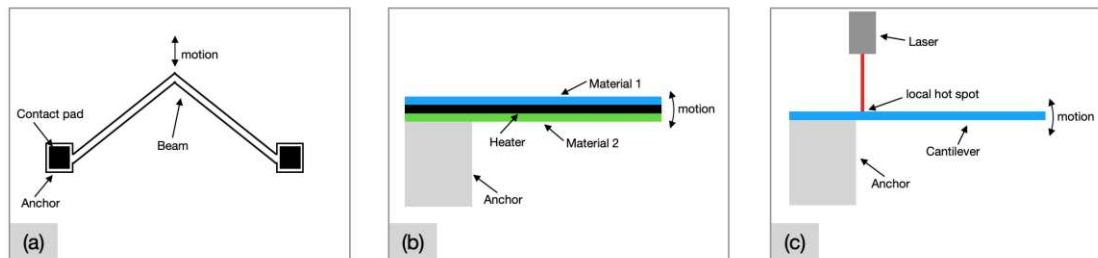


**Figure 2.11:** Examples of thermal actuation: free beam clamped on both sides (a), a heating element which is surrounded by different materials (bi-material actuator) (b), a laser causes localized heating of a cantilever, resulting in its deflection (c)

## 2.2.2 Electromagnetic Actuation

A conductor carrying an electrical current  $I$  exposed to a magnetic field  $B$  experiences the Lorentz force  $F_L$  as in:

$$\vec{F}_L = I\vec{l} \times \vec{B}. \quad (2.12)$$

This principle is very often used in macroscopic structures, for example in voice coil drivers or electric motors. To actuate a cantilever, an electrically conductive layer can be placed on top of the resonator and by applying an external magnetic field, the tip gets deflected (Figure 2.12). The advantages of such a system include the large deflections that can be achieved. One disadvantage is the external magnetic field, generated usually by a permanent magnet which has to be placed manually near the device. Another problem is that windings for micro structures are difficult to fabricate, especially horizontally on top of each other.

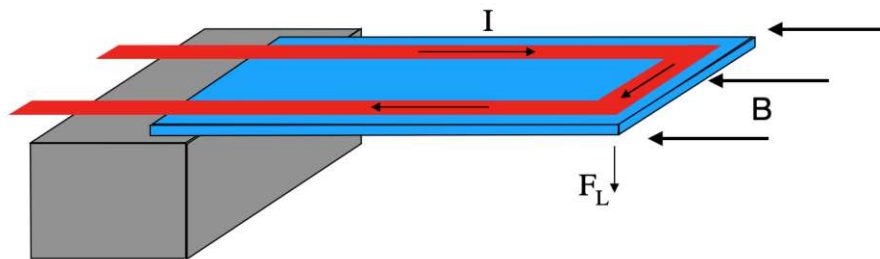


**Figure 2.12:** Electromagnetic actuation of a cantilever: by applying current to the conductor (red path), the external magnetic field ( $B$ ) causes the cantilever (blue) to bend ( $F_L$ ). A quite similar device was fabricated in [9].

## 2.2.3 Piezoelectric Actuation

Piezoelectricity is an effect in which mechanical stress on a material causes electric polarization (Figure 2.13). In reverse, an electric field causes a mechanical strain in such a material. Examples of materials used here are quartz, polyvinylidene fluoride (PVDF) and aluminum nitride (AlN). Piezoelectric actuators generally have the disadvantage that they require high voltages for relatively small changes in length, although these are often sufficient for micro systems. In [10], for example, AlN layers were deposited on cantilevers to actuate different modes. The disadvantage of such actuators, however, is the complex fabrication and that these layers cause a significant change in the properties of the underlying resonator.

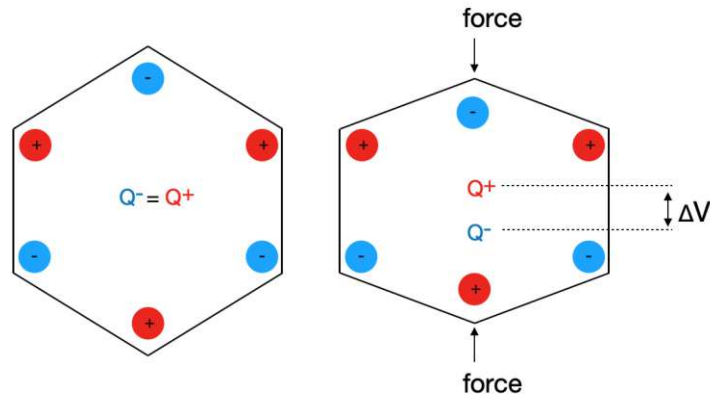


**Figure 2.13:** Structure of a piezoelectric material: without an external force, the charge centers are in the same position; if an external force is applied, the charge centers separate and an electric field is created

## 2.2.4 Electrostatic Actuation

Electrostatic actuators employ the force of attraction between two oppositely charged parts.

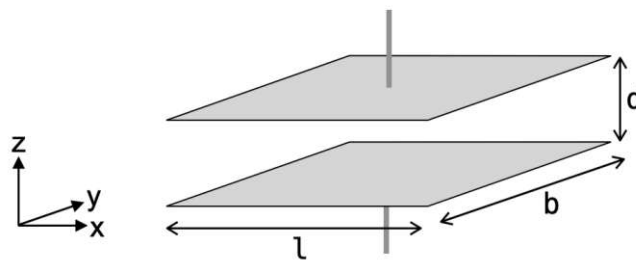


**Figure 2.14:** The two plates of a capacitor are pulled towards each other by the electrostatic force if a voltage is applied.

A suitable example is a plate capacitor as shown in Figure 2.14. Neglecting edge effects, the capacitance can be expressed by

$$C = \epsilon_0 \epsilon_r \frac{lb}{d}. \quad (2.13)$$

The energy stored in the capacitor can be calculated according to

$$E = \frac{1}{2} CU^2 = \epsilon_0 \epsilon_r \frac{1}{2} \frac{lb}{d} U^2. \quad (2.14)$$

The derivation of the energy in z-direction results in the attractive force of the capacitor plates to each other

$$F_z = \frac{\partial E}{\partial z} = -\epsilon_0 \epsilon_r \frac{lb}{2d^2} U^2. \quad (2.15)$$

If the plates have an offset relative to each other, as shown in Figure 2.15, the force

$$F_x = \frac{\partial E}{\partial x} = \epsilon_0 \epsilon_r \frac{b}{2d} U^2 \quad (2.16)$$

acts in x-direction. Since the fabrication of plate structures is relatively simple, this type of actuator is very often used for MEMS.

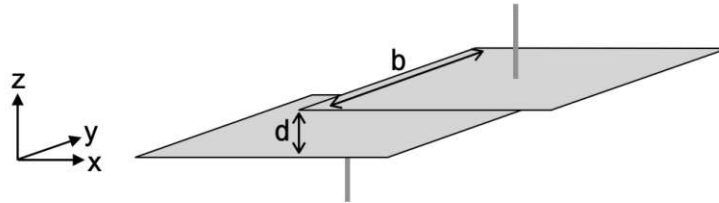


**Figure 2.15:** When the two plates are offset, the electrostatic force acts in the direction of this offset.

In order to be able to use this principle as an actuator, a force is required that is opposed to the electrostatic force, which is often accomplished with mechanical springs.

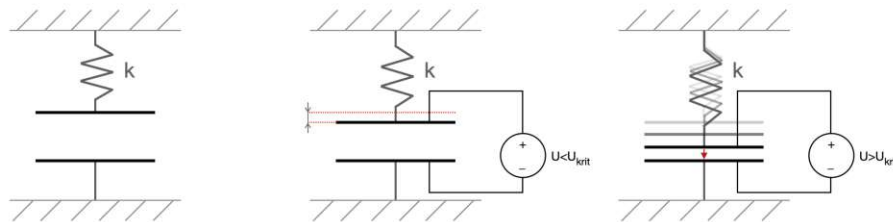


**Figure 2.16:** Pull-in effect: The position of one electrode can be changed via the electrostatic force if one electrode of the capacitor is attached to a spring. However, if this exceeds a critical point, the spring can no longer counteract and the plates collide.

Considering a plate capacitor coupled to a mechanical spring (Figure 2.16), an applied voltage generates an electrostatic force between the plates which brings the plates closer together and this again increases the force since the reduced distance increases the electrostatic force even further. The mechanical spring counteracts this, however, if the plate position exceeds a certain point, the electrostatic attraction becomes so strong that the spring is no longer able to counteract this mechanically. The plates would therefore continue to move towards each other until they touch. This is referred to as the pull-in effect, which restricts the actuator's travel to only one-third of the distance between the plates in their neutral position.

If this spring-coupled capacitor also has a low level of damping, the system is characterized by a resonant frequency with a certain  $Q$ -factor. Exciting this system with a voltage consisting of a DC voltage component and an AC voltage prevents frequency doubling phenomena, which would otherwise result from the quadratic relationship between the force and the voltage. As a result, the force on the plate is composed of

a constant attractive term and a time variable term. In the resonant case, only the alternating part of the force causes the periodic deflection of the plate. The RMS (root-mean-square) of the force is not proportional to the square of the AC voltage, but rather directly proportional to it. Therefore the resulting deflection at the resonant frequency varies linearly with the applied amplitude of the AC voltage. This observation is applicable only for minor displacements around the equilibrium position of the plate, where the force remains relatively constant despite alterations in the distance between the plates.

Since the production of electrostatic actuators is relatively simple and promises to reach high frequencies, this type of actuation is implemented in this work.

## 2.3 Concept for Electrostatic Actuation

In order to be able to actuate a cantilever using electrostatic forces, the cantilever must either be intrinsically conductive (e.g. doped) or have a conductive layer applied to it. In addition, a second electrode must be placed stationary in an area that results in an electrostatic force which deflects the cantilever in the desired direction.

Cantilevers made from electrical insulators are used for MEMS relays, as an example [11]. A representation of such a structure is shown in Figure 2.17. Stress, which usually originates from the manufacturing of the layer, causes the cantilever to bend upwards after the release. The gap between the cantilever and the bottom electrode is usually created by wet chemical etching. However, this process can cause the cantilever to stick to the bottom electrode, which is generally known as sticking [12]. By omitting the switch contacts, this structure can be used to fabricate electrostatically actuated cantilevers.

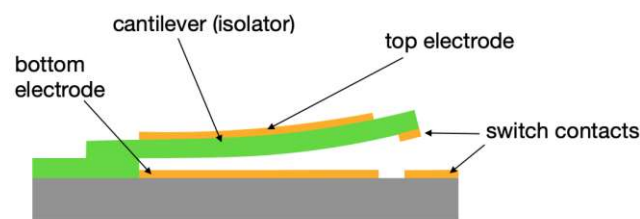


**Figure 2.17:** Model of a MEMS relay: if a sufficiently high voltage is applied between the metal layer on the cantilever and the electrode underneath, the switch at the front makes contact. The wiring to the electrodes and to the contacts of the switch are not illustrated.

To avoid wet etching, an alternative method is to fabricate the cantilever and the electrode separately and then join them together to form a single device Figure 2.18. However, this process has the disadvantage that the alignment must be very precise and that the cantilever can touch the top of the electrode if there is too much stress in the layer.

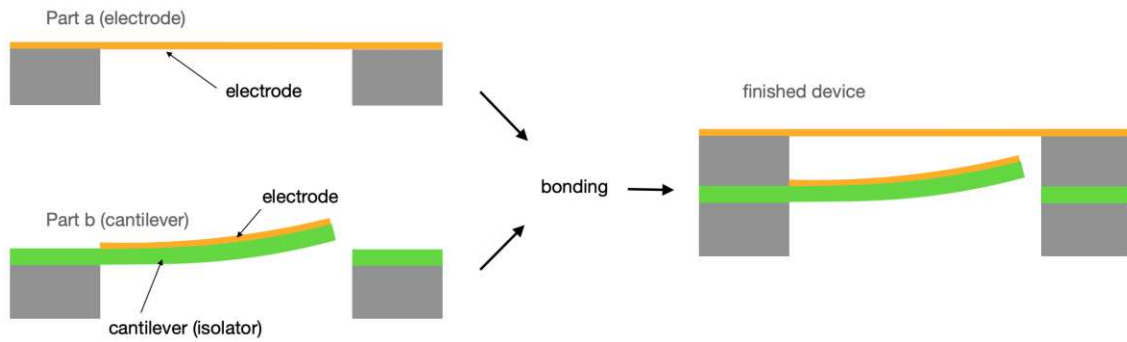


**Figure 2.18:** Separate fabrication of the cantilever and the electrode eliminates the need for wet etching. However, joining the two parts together requires a high degree of precision.

In [13], cantilevers were fabricated with electrodes on the side (Figure 2.19), which greatly simplifies the manufacturing process. In addition, no pull-in effect can occur as the electrodes never come into contact with the cantilever.

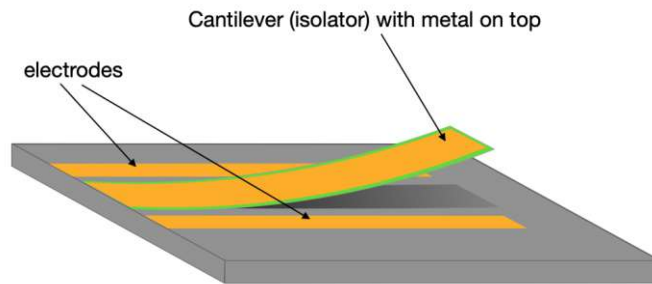


**Figure 2.19:** Electrodes situated to the sides of a Cantilever are easy to fabricate and have the advantage of avoiding pull-in effects.

By placing the fixed electrode opposite the cantilever instead sideways, the cantilever can be released through a hole etched from the back and wet chemical etching is no longer necessary (Figure 2.20). This also has the advantage that the electrostatic force acts very localized on the front area of the cantilever and therefore various modes can be actuated.

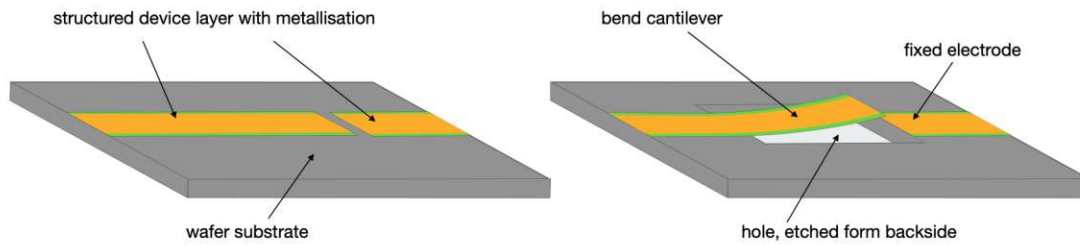


**Figure 2.20:** Design approach employed for this work: Electrode and resonator are fabricated in one plane (left), after etching a hole from the backside, the resonator experience a stress induced bend, and therefore out-of-plane modes can be electrostatically actuated (right).

# 3 Transducer Principle and Experimental Details

## 3.1 Placement of the Electrodes

In order to achieve electrostatic actuation as described in Section 2.3, certain parts of the resonator structure must obtain a certain electrical conductivity. Both, undoped and doped polycrystalline materials should be used for the cantilevers. In the case of undoped materials, the cantilever is coated with a thin, conductive metal layer. In the instance of the doped materials, only the electrode in the anchor region is coated with a suitable metal so that an ohmic contact is created and the doped cantilever can act as an electrode. To measure the electrical conductance of the doped layer, a dedicated structure is applied to the doped wafers (more on this measurement method in Section 3.7).

A mode cannot be actuated, if an external force acts on a point that is located on a nodal line of this mode. In order to achieve as much deflection as possible, the force should act on one of the points of the cantilever that has the most deflection for this mode. However, as the electric field between the cantilever and the opposing electrode is never concentrated on exactly one point, the force acts not only on one point but on the entire cantilever width, although this is always dependent on the distance between the respective point on the cantilever and the opposing electrode. Therefore, the following two different designs were developed.

### 3.1.1 Single Electrode

For this particular configuration, the counter electrode is placed exactly opposite the cantilever at a distance of  $3\mu\text{m}$  (see Figure 3.1). For the modes M10, M20 and M30, the front edge of the cantilever has the greatest deflection. On the other hand, mode M11 (torsion mode), should not be possible to actuate, as the deflection of the corners is always in anti-phase, but the electrostatic force acts in phase on the entire edge.

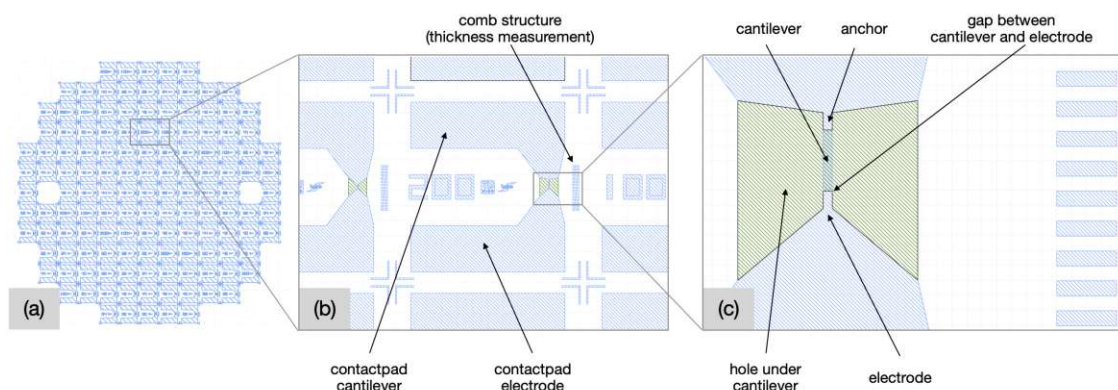


**Figure 3.1:** Single electrode design: (a) complete mask overview, (b) single component with  $200\mu\text{m}$  overhang, (c) magnification of the same cantilever

### 3.1.2 Dual Electrode

In order to actuate other modes as well, the electrodes in this configuration (Figure 3.2) are placed so that the force does not act uniformly on the front edge. Electrode 1 acts very locally on an area around the left corner of the cantilever and electrode 2 on a larger area on the front edge, but with a shift to the right. It should be noted here that the two electrodes are not electrically connected and can be operated separately or connected together externally. The small electrode (Figure 3.2 - electrode 1) should be able to actuate all modes, as the maxima of each mode can always be found on one of the corners. However, the electrostatic force with this electrode design will be smaller compared to one big electrode, as the effective capacitor area is much smaller here, and therefore the force on the cantilever is also smaller. In order to achieve a greater force, the large electrode (Figure 3.2 - electrode 2) is added. The effective capacitor between electrode 2 and cantilever is almost as large as that of the single electrode design, but due to the shift from the center, the force acts stronger on one side of the cantilever. The modes M10, M20 and M30 should be almost as easy to excite as in Design 1, but M11 can also be actuated, as the force here acts more strongly on the right-hand side.

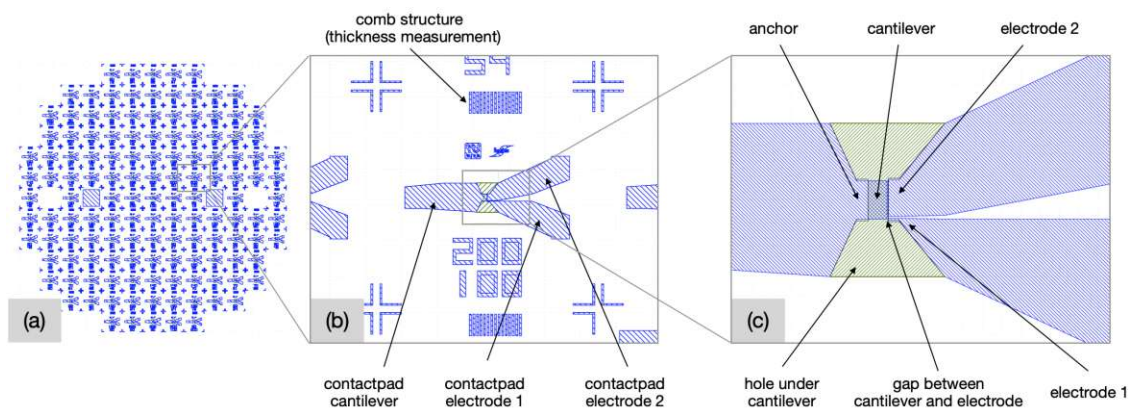


**Figure 3.2:** Dual electrode Design: (a) complete mask overview, (b) single device with  $200\mu\text{m}$  width and  $100\mu\text{m}$  overhang, (c) magnification of the same cantilever

To release the structure, the silicon substrate under the cantilever has to be removed. This is done by reactive ion etching (see Section 3.4.1.5). Theoretically, a rectangular region enclosing the cantilever would work for this procedure, however, for process reasons, the opening is deliberately widened on both the left and right of the cantilever (green area in Figure 3.1 and Figure 3.2). This expansion is essential to ensure a uniform and consistent ion flow during the etching within the designated region.

### 3.1.3 Layer Thickness Variation

Some of the polycrystalline coated wafers exhibit significant variations in thickness, with deviations of up to  $\pm 50\%$  in comparison to the baseline thickness. Given the inherent heterogeneity of these coating layers, which varies from one wafer to another, a comb structure (as marked in Figure 3.1 and Figure 3.2) is introduced alongside each

individual component. This addition served the purpose of facilitating a precise post-production assessment of the layer thickness in proximity to the corresponding component.

## 3.2 Description of the Measuring Equipment

For the subsequent measurements of the fabricated devices, various methods and instruments are used, which are described in the following sections.

### 3.2.1 Scanning Electron Microscope

A scanning electron microscope (SEM) uses a focused electron beam that is moved across the surface of a sample in a vacuum. The interaction between the electrons and the sample produces various signals such as secondary electrons, backscattered electrons and X-rays. Detectors record these signals and convert them into electrical signals. These signals are then processed to generate an image of the surface of the sample. The raster scanning of the sample produces a high-resolution image that shows the topographical and structural features of the sample. The high resolution ability of the SEM, which can reach up to a few nanometers, makes it possible to observe and study nanostructures with great precision. The Hitachi SU8030 is the specific instrument that was employed for this work.

### 3.2.2 Profilometer

The profilometer uses a scanning step method for the metrological description of the surface of a sample. A diamond needle is positioned on the sample with a previously defined vertical contact force. The needle is then moved over a defined distance and the contact force is kept constant (see fig. 3.3). If the topology changes, the controller readjust the actuator for the contact force, and this results in information about the sample profile. A Bruker DektakXT Surface Profiler is used for the surface measurements conducted in this work.

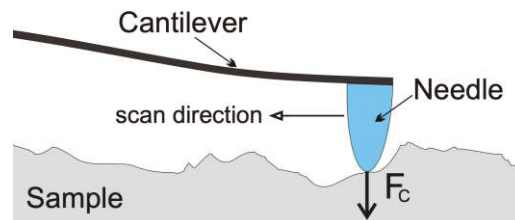


**Figure 3.3:** Basic principle of a profilometer: the cantilever (black) with the diamond tip (blue) is moved over the sample (gray) while the force ( $F_c$ ) on the sample is kept constant.

### 3.2.3 Laser-Doppler Vibrometer

The laser-doppler vibrometer uses the frequency change that light experiences when it is reflected by a moving surface, i.e. the doppler effect. The basic structure of such a measuring system is shown in Figure 3.4. The laser generates monochromatic, coherent light with a fixed reference frequency which is split into 2 beams at the beam splitter 1. The measurement beam goes to the moving sample and undergoes a frequency change upon reflection. The reflected beam interferes with the unchanged reference beam via beam splitter 3 and is converted into an electrical measurement signal at the detector. The Bragg cell is used to modulate the reference frequency in order to detect the sign of the measured velocity. The Polytec MSA 500 used for this work allows measurements in velocity mode up to 2 MHz, and up to 20 MHz in deflection mode.

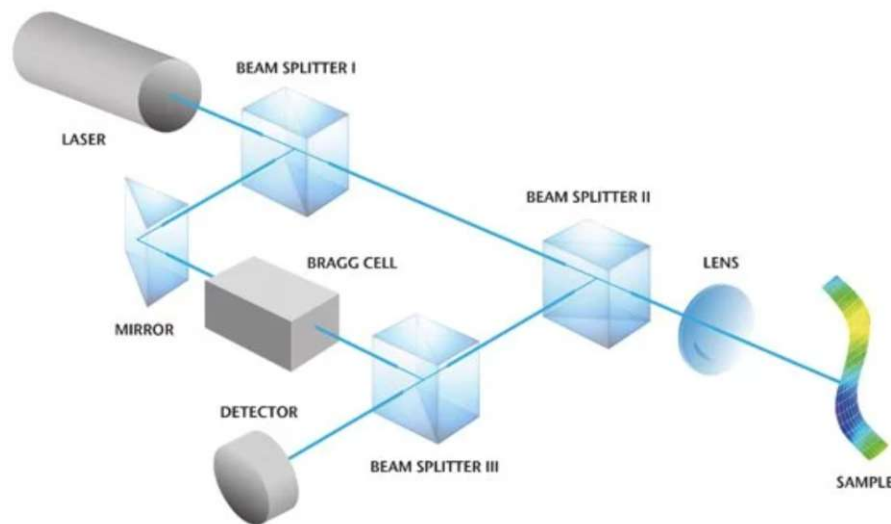


**Figure 3.4:** Functional principle of a laser-doppler vibrometer [14]

### 3.2.4 Lock-In Amplifier

A lock-in amplifier can extract the amplitude and phase of a chosen frequency from signals with high noise levels. The operating principle is shown in a simplified form in Figure 3.5. Basically, the measuring device works according to the mathematical properties of the multiplication of two equal-frequency but phase-shifted sinusoidal signals. The frequency to be measured is generated at a local oscillator, phase-shifted and multiplied with the input signal after it has been amplified and band-pass filtered. If the noisy measured sinusoidal signal is in phase with the reference signal, the DC component of the multiplication of the two is maximized. Since the mean value of noise is zero, the error of the measurement decreases with a longer integration time. Assuming the measurement is long enough, a signal can be measured that is decades smaller than the superimposed noise.

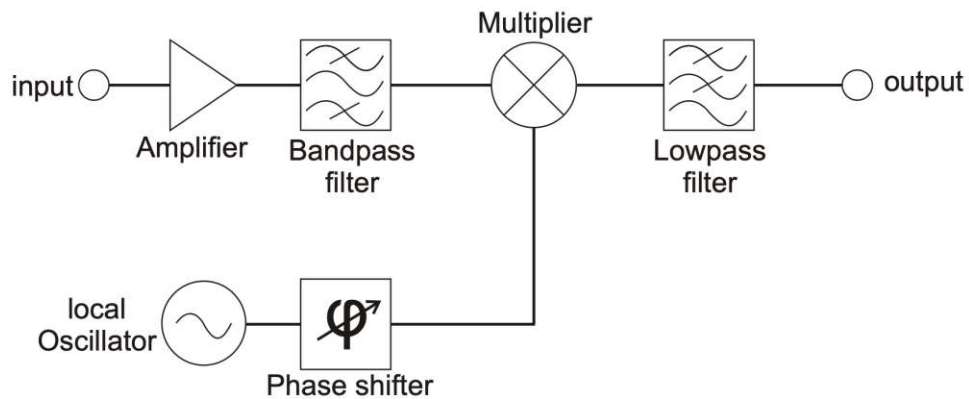


**Figure 3.5:** Simplified representation showing the signal path of a lock-in amplifier: The noisy signal to be measured is amplified and bandpass filtered around the frequency set on the local oscillator. By multiplying the filtered input signal with the phase-shifted oscillator sinusoidal signal, a DC loaded signal is generated. After lowpass filtering, the DC component remains, the amplitude of which corresponds to the amplitude of the input signal hidden in the noise at the oscillator frequency.

### 3.2.5 Laserdriver

A laser with a maximum optical output power of 2.5mW, controlled by a driver is utilized for the photo-thermal actuation of the cantilevers. The laser driver (Thorlabs CLD1010, Figure 3.6) is controlled via a voltage signal and sets a corresponding current at the laser diode. In addition, a temperature controller is integrated, which keeps the temperature of the laser diode constant and thus ensures that the given current always produces the same laser output power.



**Figure 3.6:** Laser controller: the temperature of the laser diode is kept constant at 25°C while the laser current is controlled with an external voltage signal.

### 3.3 Device Layer Materials

The materials used for the resonators are polycrystalline thin films. Each wafer is coated with a layer of the respective polycrystalline material (in the range of 1.5  $\mu\text{m}$ -4  $\mu\text{m}$ ). The following materials were used for the resonators measured in this work:

#### Polycrystalline Silicon

Polycrystalline silicon (polySi) is a standard material in the semiconductor industry. PolySi is typically deposited using low-pressure chemical vapor deposition (LPCVD) [3]. In this process, silane pyrolytically forms a polycrystalline layer on the wafer surface in a low-pressure chamber at temperatures of around 600 °C. The properties of such a layer depend heavily on the grain size and orientation of the individual grains, which is controlled by process parameters such as pressure and temperature.

The polySi coated wafers used for this work were manufactured by Hahn-Schickard-Gesellschaft für angewandte Forschung e.V. The manufacturer specified a deposition temperature of 570 °C and a layer thickness of 2000 nm  $\pm$ 10%. An image of the surface is shown in Figure 3.7.

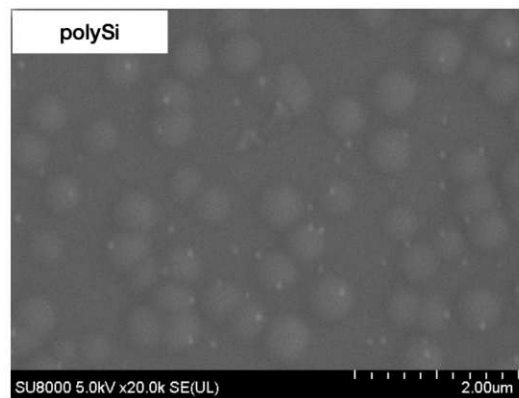


**Figure 3.7:** SEM image of the polySi surface topography.

### Polycrystalline Diamond

Similar to polySi, the material is deposited in a low-pressure chamber, but here a so-called hot filament chemical vapor deposition process (HFCVD) is used [15]. The deposition of these layers was carried out by the company CarbonCompetence GmbH. They use tantalum rods, which are electrically heated to 2400 °C and hydrogen and methane are directed into the chamber over the filament. The wafer is seeded with diamond nano particles with an average size of 5 nm and the chamber pressure during the process is approx. 5 mbar. In this way, polycrystalline diamond layers several micrometers thick can be deposited. By precisely adjusting some of the process parameters, it is possible to deposit different grain sizes. A rough distinction is made here between microcrystalline diamond (mdiamond) and nanocrystalline diamond (ndiamond). Figure 3.8 shows the difference in grain size between the two different layers. It is also technically possible to fabricate doped layers, for example with the dopant boron. The deposited layers had thicknesses of around 2 - 4 μm, with a pronounced thickness gradient across the wafer in some cases.

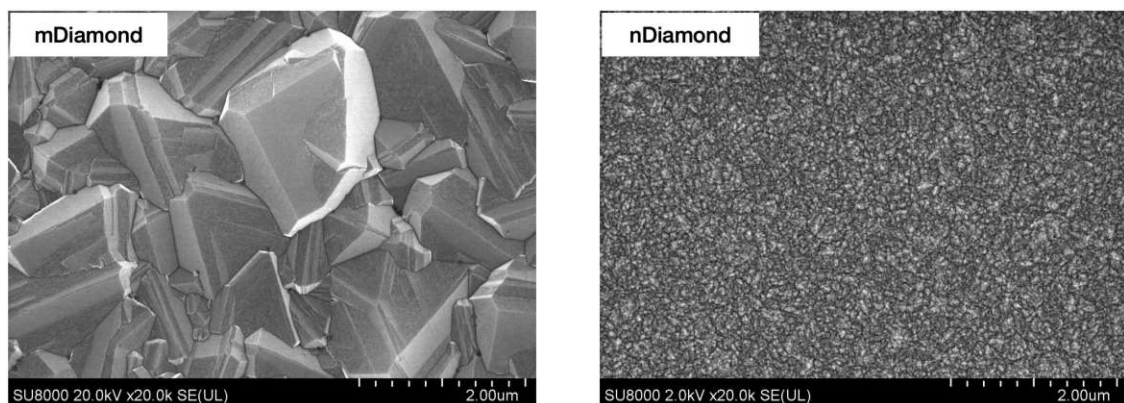


**Figure 3.8:** Difference between the grain sizes of mdiamond and ndiamond

## 3.4 Fabrication Parameters and Settings

All the processes and equipment used to fabricate the components are described in the following sections. Section 3.4.2 and Section 3.4.3 describe the detailed fabrication process for undoped and doped layers respectively.

### 3.4.1 Technologies

#### 3.4.1.1 Photolithography

Optical lithography is used in microsystem technology to create small, complex structures. A photoresist applied to a wafer is partially shaded using a mask and therefore only individual areas are chemically changed during exposure. After the development, these resulting small patterns on the wafer can then be used to cover small dedicated areas with a thin film, or as an etching mask. The steps to transfer a mask design to a wafer are described in more detail in the following.

##### **Cleaning**

Contamination of the wafer can massively affect the quality of the final coating layer. Therefore, the wafer is cleaned first, which can be done with a fully automatic wafer cleaner, which rinses the wafer with deionized water (DI-water) and ultrasonic waves.

##### **Coating**

The wafer is placed on a spin-coater, photoresist is applied and a previously defined maximum rotation speed ensures that the coating is homogeneously distributed over the entire wafer. The final thickness of the resist is controlled via the maximum rotational speed of the wafer.

##### **Softbake**

The spin-coated wafer is placed on a hotplate at a specific temperature for a specific time, which are both predefined by the datasheet of the photoresist. This step causes residual water in the resist to evaporate.

##### **Mask exposure**

Here, the actual structure is transferred to the resist via the mask. The mask is made of glass on which the desired microstructures are vapor-deposited with chromium (Figure 3.9). In the exposure device, the mask is pressed on to the wafer and exposed to UV light for a certain period of time. Those areas that are not covered by the chromium layer on the mask undergo a photochemical reaction. After this reaction, the exposed part of the resist behaves differently to the unexposed part during further chemical treatment. If negative resist is used, the exposed areas become insoluble for the chemical developer, with positive resist it is exactly the opposite, as illustrated on the right in Figure 3.9. In case some structures have already been deposited on the wafer, the mask must be aligned using the alignment marks on the wafer and the ones on the mask before exposure.

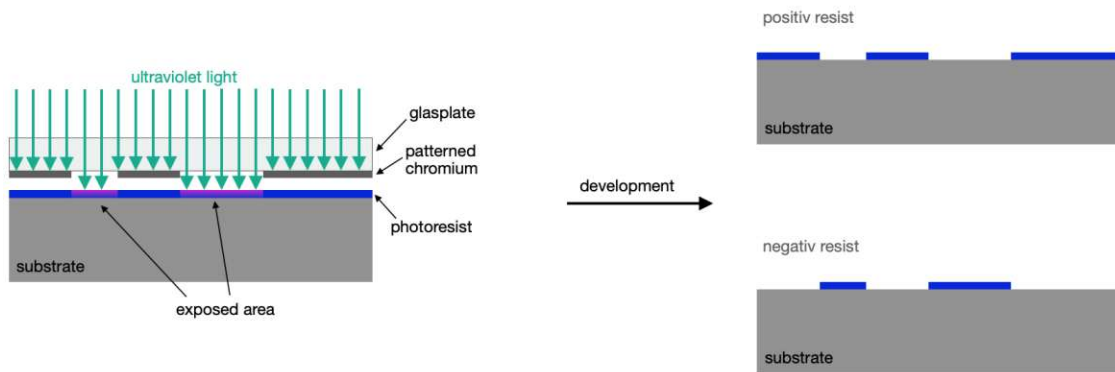


**Figure 3.9:** Mask exposure: The mask blocks the ultraviolet light in certain areas. The exposed areas behave differently for negative or positive resists.

### Hardbake

If a negative photoresist is used, the Wafer is placed again on the hot-plate to further solidify the resist, which makes the layer more durable.

### Flood Exposure

Further exposure of the negative photoresist ensures that the polymer chains formed by the first exposure crosslink even further and are not attacked as strongly during the development of the resist.

### Development

For the development, the wafer is processed in an automated machine with DI water and a chemical developer. The program sequence follows the respective recipe of the photoresist, and thus dissolves the parts of the resist from the surface that did not receive a sufficient chemical transformation during the previous steps.

#### 3.4.1.2 Metal Evaporation

A standard method for fabricating thin films is evaporation. Figure 3.10 shows the simplified structure of this type of system. The wafer is placed in a vacuum above the material to be vaporized. A heater brings the material to be evaporated (e.g. gold) to such a high temperature that it becomes vaporized and as there is a high vacuum in the chamber, the vapor can spread almost freely. For some materials, an electron beam can be used instead of the heater to vaporize the metal (e.g. aluminium). On contact with the much cooler wafer, the metal condenses on the surface, slowly forming a thin film. If a partial masking of the surface was previously produced on the wafer (for example with a photoresist), the metal is also deposited on the mask. If the mask is removed later, only the metal layer remains on the previously open areas of the mask.

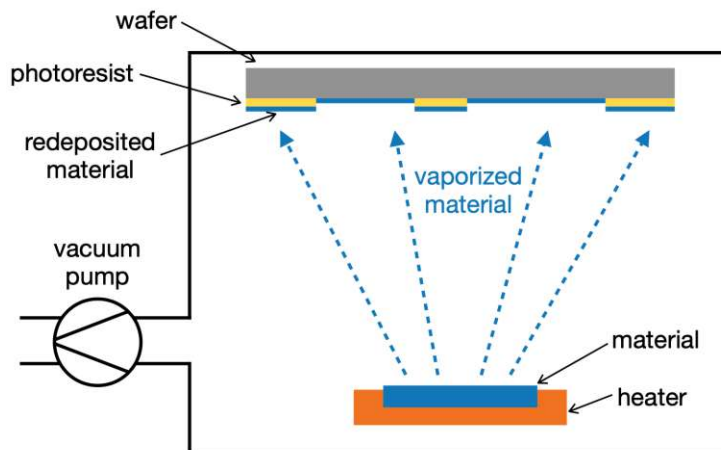


**Figure 3.10:** Simplified illustration of a thermal evaporation plant

### 3.4.1.3 Lift-Off

After vapor deposition of the metal layer, all metal that has been deposited on the photoresist must be removed (Figure 3.11). To do this, the wafer is completely immersed in a heated acetone solution and treated with ultrasound. The acetone dissolves the photoresist and the cavitation bubbles created by the ultrasonic waves lift the metal from the resist to prevent sticking. After most of the photoresist has been removed, the wafer is placed in a fresh acetone solution and the process is repeated. Once all areas are free of photoresist and unwanted metal, the wafer is then cleaned in an isopropanol solution and air-dried.

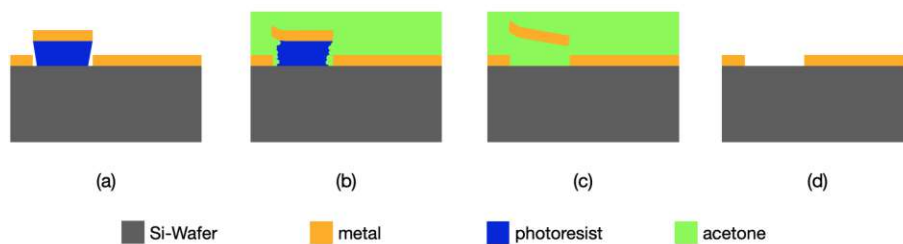


**Figure 3.11:** After depositing the metal layer (a), the photoresist is dissolved with acetone and the aid of ultrasonic waves (b). After complete dissolution of the photoresist (c), the wafer structured with metal remains (d).

### 3.4.1.4 Reactive-Ion Etching

Reactive-ion etching (RIE) is a dry etching process, where gases are introduced into a reaction chamber under vacuum and an electrical field ionizes the molecules. The resulting high-energy ions react with the wafer surface and remove material. This technique can be used for both, isotropic and anisotropic etching. By controlling the electric field,

the ions can be directed onto the wafer and thus a more anisotropic etching profile is achieved.

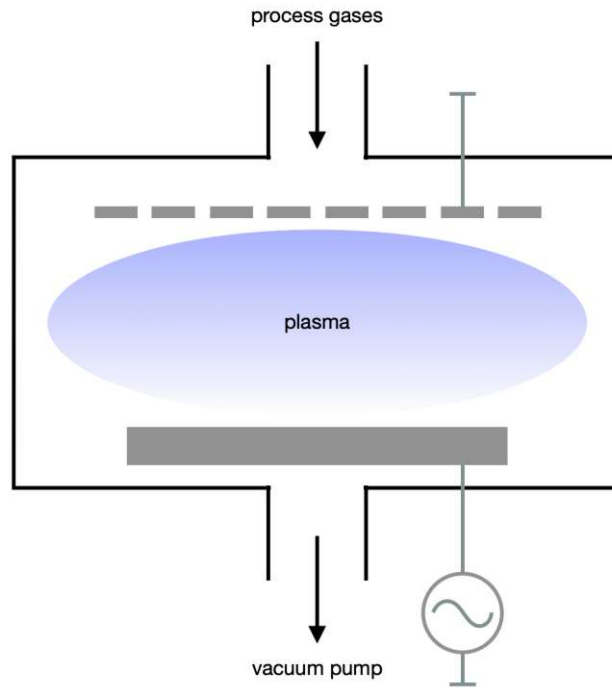


**Figure 3.12:** System overview of an RIE plant

#### 3.4.1.5 Deep Reactive-Ion Etching

If high aspect ratios are required, RIE quickly reaches its limits. A further development of RIE is deep reactive-ion etching (DRIE), which was developed by Bosch [3] and is therefore also known as the Bosch process. The process consists of two sub-steps, the actual etching and a passivation step. During etching,  $\text{SF}_6$  and argon as a carrier are introduced into the chamber and ionized into a plasma, which attacks the unmasked silicon substrate (Figure 3.13 b). After just a few seconds, this step is stopped and a passivation step is initiated.  $\text{C}_4\text{F}_8$  and argon are fed into the chamber and the plasma is ignited. This forms a polymer passivation layer on the surface of the wafer, which protects its surfaces (Figure 3.13 c). The following etching step (again  $\text{SF}_6$  and argon) attacks the polymer protection layer of the side walls much less than the horizontal surfaces (Figure 3.13 d), whereby the etching trench spreads mainly into depth. The constant alternation of the two steps (etching and passivation) results in deep etching trenches with almost vertical side walls.

#### 3.4.1.6 Hydrofluoric Acid (HF) Dip

Beneath the device layer is a 500nm thick layer of  $\text{SiO}_2$ , which acts both as an etch stop in the previous dry etching processes and as an electrical insulator for the later

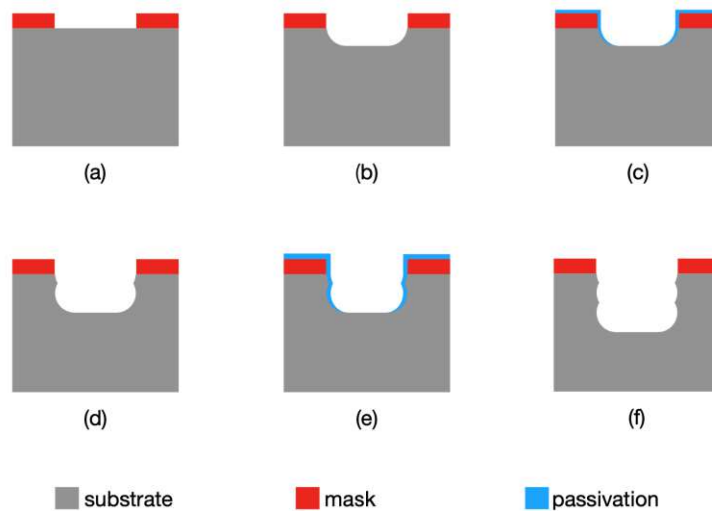


**Figure 3.13:** basic operating principle of deep reactive ion etching (Bosch-process)

device. To remove the  $\text{SiO}_2$  under and around the cantilever, the wafer is immersed in a solution of hydrofluoric acid (HF) and  $\text{NH}_4\text{F}$  (called buffered HF). This dissolves the  $\text{SiO}_2$  and ensures the final release of the cantilever.

### 3.4.2 Fabrication Steps for Undoped Materials

The fabrication steps for undoped material are described for undoped polycrystalline diamonds. First, a resist mask is applied to the device layer (Figure 3.14 a). Using thermal evaporation, 20 nm titanium is vapor-deposited as an adhesion enhancer for the 80 nm gold electrode. In order to protect the gold during the following etching process of the device layer, 400 nm aluminum is deposited as a hard mask. Following the liftoff process (Figure 3.14 c), the diamond layer is etched, using the DRIE with alternating steps of  $\text{O}_2$  and  $\text{O}_2/\text{CF}_4$  according to [16]. After this front side etching (Figure 3.14 d), the back side mask is imposed on the wafer and the front side is completely passivated with a continuous resist layer (Figure 3.14 e). The deep etching of the backside is again done with the DRIE according to the Bosch process (Figure 3.14 f). To remove the electrically insulating  $\text{SiO}_2$  layer under the cantilever, the wafer is briefly immersed in HF (Figure 3.14 g). After sawing the wafer into strips, the photoresist is removed with acetone, isopropanol and then with oxygen plasma using the RIE. Finally, the aluminum hard mask is stripped off with a chemical aluminum etch (Figure 3.14 h).

Components made of undoped poly silicon are also produced. For these components, a photoresist mask is used instead of the aluminum hard mask, as the front side etching of poly silicon was carried out with the Bosch process, in contrast to  $\text{O}_2/\text{CF}_4$  as with diamond. The basic fabrication process as shown in Figure 3.14 otherwise remained the same.

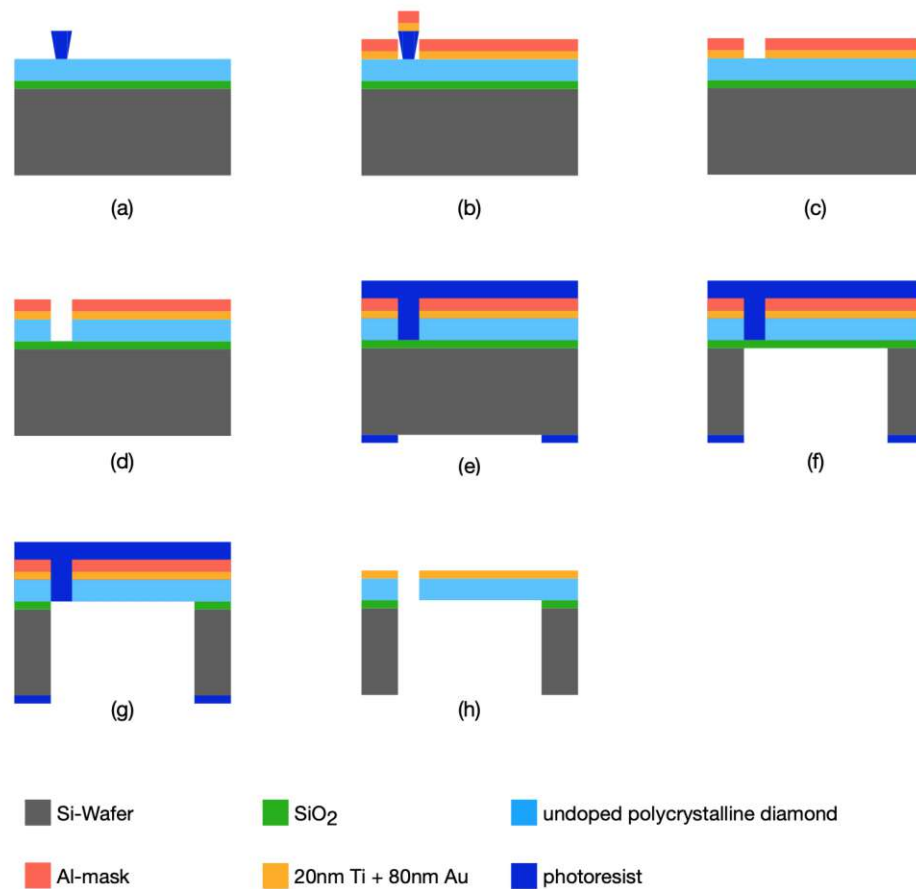


**Figure 3.14:** Fabrication steps for undoped polycrystalline diamond

### 3.4.3 Fabrication Steps for Doped Materials

The fabrication steps for doped materials are almost the same as for undoped materials. However, the mask for contacting and the mask for frontside etching are different for doped materials. In the first step, the mask for the ohmic contacts are applied (Figure 3.15 a), which does not include the cantilever, but only goes as far as the anchor. Then 20nm titanium and 80nm gold are vapor-deposited (Figure 3.15 b), followed by a liftoff process (Figure 3.15 c). To etch the front side, another hard mask made of aluminum is required. This is done with a second mask, which covers all surfaces coated with titanium/gold and also the cantilever (Figure 3.15 d and e). After etching the front side, the following steps are the same as for the undoped material (Figure 3.15 f-i). First the backside mask is applied and the front side passivized, then the backside of the wafer is etched in depth using the Bosch process. After the following HF dip, the wafer is sliced into strips and the resist is first cleaned with acetone and isopropanol. After removing any resist residues with O<sub>2</sub> plasma in the RIE, the aluminum hard mask is finally chemically removed.

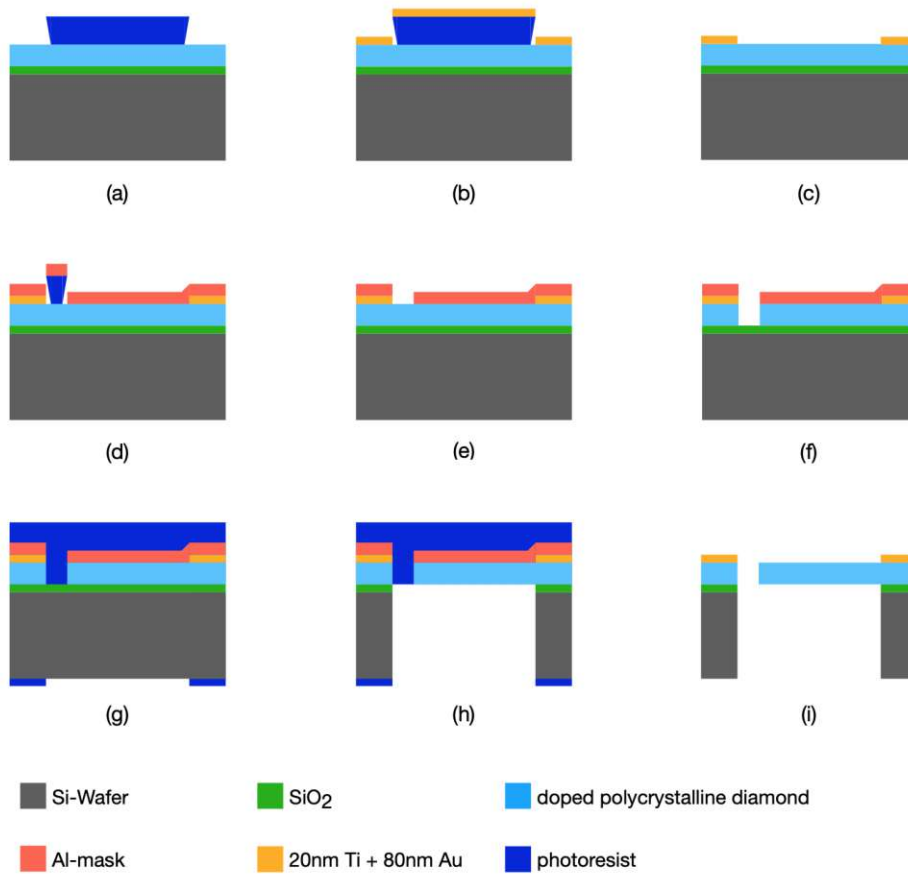


Figure 3.15: Fabrication steps for doped polycrystalline diamond

process step	dual electrode design			single electrode design
	polySi	poly mdiamond	doped mdiamond	n diamond
<b>lithography device layer</b>	front side mask 2 (negative resist)	front side mask 2 (negative resist)	front side mask 1 (negative resist)	front side mask (negative resist)
<b>metal evaporation</b>	20nm Cr / 80nm Au	20nm Ti / 80nm Au / 400nm Al	20nm Ti / 80nm Au	20nm Cr / 80nm Au / 400nm Al
<b>lift off</b>	acetone / isopropanol	acetone / isopropanol	acetone / isopropanol	acetone / isopropanol
<b>lithography device layer</b>	front side mask 2 (positive resist)		front side mask 2 (negative resist)	
<b>metal evaporation</b>			400nm Al	
<b>lift off</b>			acetone / isopropanol	
<b>RIE device layer</b>	bosch etching	diamond front side etching CF <sub>4</sub> /O <sub>2</sub>	diamond front side etching CF <sub>4</sub> /O <sub>2</sub>	diamond front side etching CF <sub>4</sub> /O <sub>2</sub>
<b>lithography handle layer</b>	back side mask (ps resist) and frontside protection resist	back side mask (ps resist) and frontside protection resist	back side mask (ps resist) and frontside protection resist	back side mask (ps resist) and frontside protection resist
<b>DRIE handle layer</b>	backside bosch etching	backside bosch etching	backside bosch etching	backside bosch etching
<b>BOX removal</b>	HF-dip	HF-dip	HF-dip	
<b>strip sawing</b>	glueing on mounting tape and sawing	glueing on mounting tape and sawing	glueing on mounting tape and sawing	
<b>mounting tape and resist removal</b>	acetone / isopropanol	acetone / isopropanol	acetone / isopropanol	acetone / isopropanol
<b>RIE resist removal</b>	O <sub>2</sub> Plasma: duration 18 min	O <sub>2</sub> Plasma: duration 18 min	O <sub>2</sub> Plasma: duration 18 min	
<b>metal etching</b>		Al etching	Al etching	Al etching
<b>final cleaning step</b>	acetone / isopropanol	acetone / isopropanol	acetone / isopropanol	acetone / isopropanol

**Figure 3.16:** Summary showing the process steps for fabricating the different device layer materials

### 3.4.4 Fabricated Devices

Several materials were fabricated with different device layers. Figure 3.17 and Figure 3.18 show some examples with various materials, both doped and undoped.

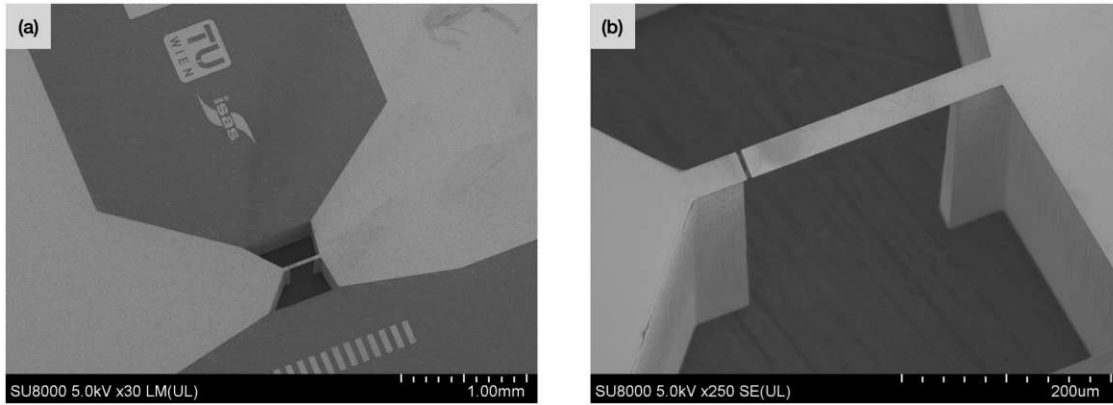


**Figure 3.17:** SEM images of the same diamond cantilever (200  $\mu\text{m}$  long, 30  $\mu\text{m}$  wide) with a single electrode

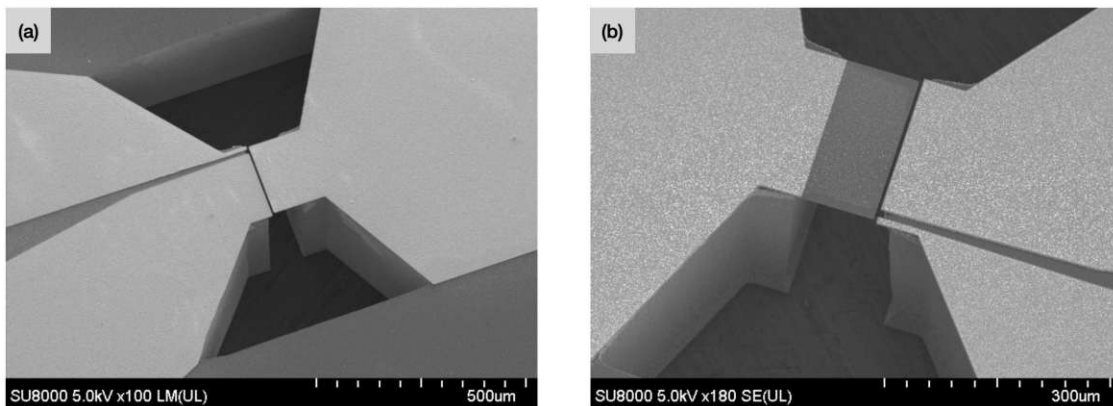


**Figure 3.18:** SEM images of fabricated plate resonators with two electrodes: undoped polySi (a) and doped monocrystalline silicone (b)

### 3.5 Measurement Setup for Resonances

In order to measure the deflection of the cantilevers at different frequencies, both photo-thermal (Figure 3.19) and electrostatic actuation (Figure 3.20) are used. The reference signal generated at the lock-in amplifier is fed either to the laser or directly to the electrode. The deflection of the cantilever is detected by the laser-doppler vibrometer and fed to the input of the lock-in amplifier.

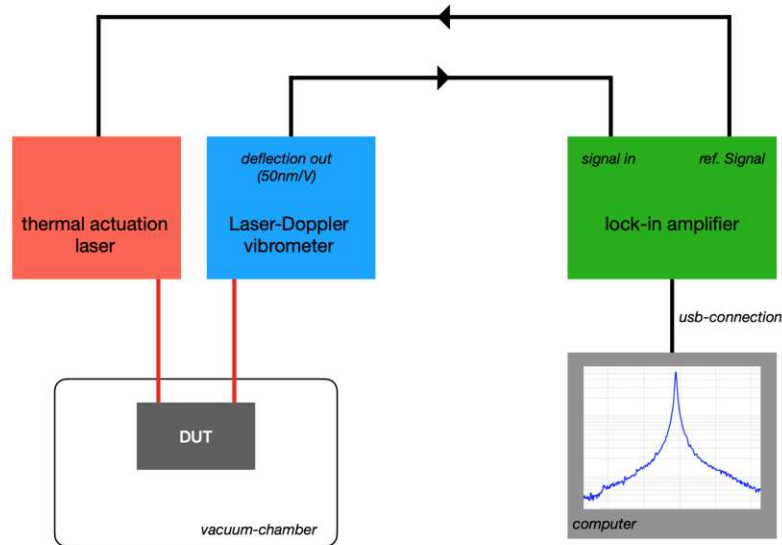


**Figure 3.19:** System setup for the deflection measurement with thermal actuation

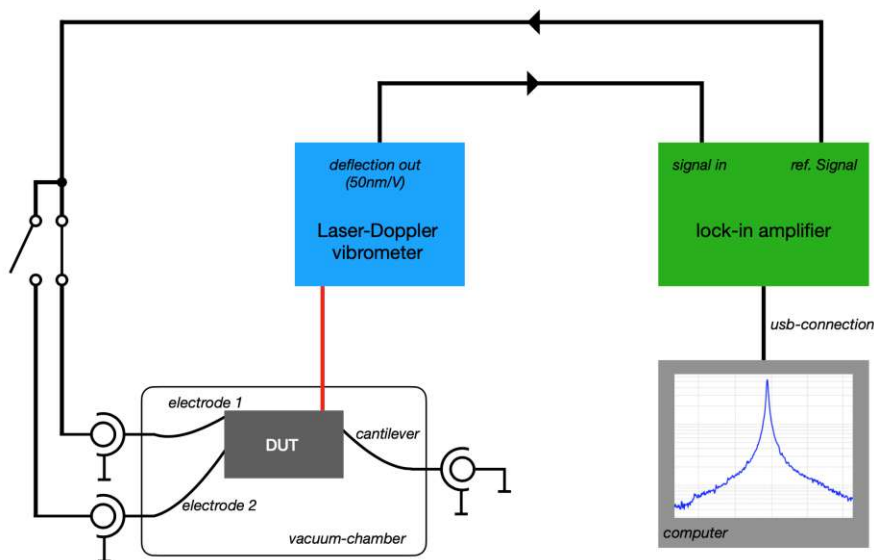


**Figure 3.20:** System setup for the deflection measurement with electrostatic actuation

### 3.5.1 Photo-Thermal Actuation

In case of actuation with the laser, the AC amplitude of the reference signal at the lock-in amplifier and the DC component is always set to the same value (Figure 3.21). As a result, the laser introduces the thermal energy into the material at the same frequency as the reference signal, whereby the heating also has an average value due to the DC offset. In order to maximize the amplitude of the respective mode, the laser spot must be positioned at an area on the cantilever where the surface stress in the material is at a maximum for the modes of interest. If the laser point is placed near a nodal line, the deflection is also minimized, therefore the laser spot is positioned close to the anchor as shown in Figure 3.22. For all the considered modes, the maximum deflection of the cantilever occurs at one of the two corners, so the measuring laser of the laser-doppler vibrometer is placed on one of the corners. The upper frequency limit of the laser driver is 300 kHz.

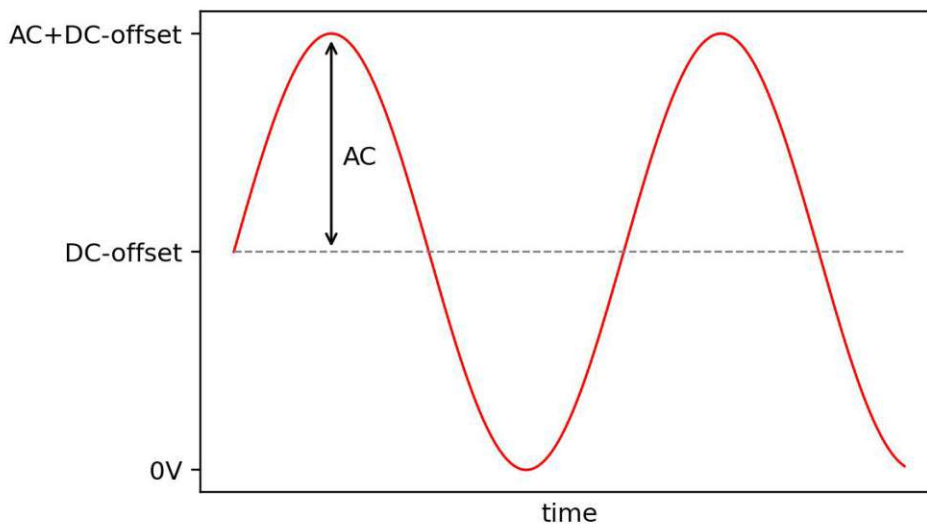


**Figure 3.21:** Signal to drive the cantilever: An ac sine wave is combined with an equal dc component, the resulting signal has a minimum amplitude of 0 V and a maximum amplitude of double the ac-peak amplitude.

### 3.5.2 Electrostatic Actuation

In order to avoid frequency doubling, the ac amplitude and the dc amplitude were also chosen to be the same for the electrical excitation. In principle, it would also be possible to feed the electrodes with an average free sine wave, although the lock-in amplifier would then have to use the second harmonic of the reference signal for further signal processing. The readout point for the laser-Doppler vibrometer is again set to the corner.

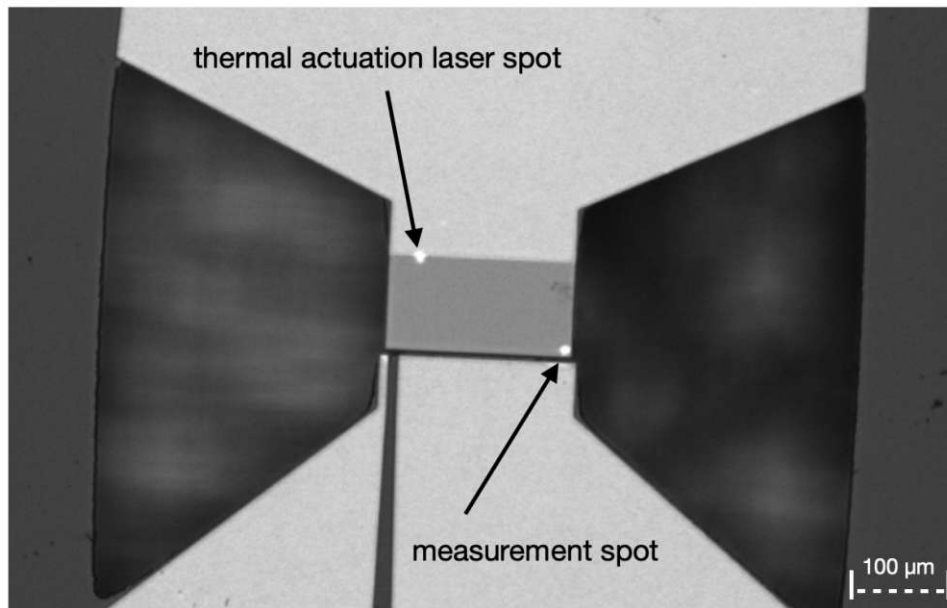


**Figure 3.22:** Position of the thermal actuation laser spot near the anchor and the measurement-laser near the right corner

## 3.6 Measurement Procedure

### 3.6.1 Electrical Contacting inside the Vacuum Chamber

Due to the limited space in the vacuum chamber, contacting individual devices on the wafer is not feasible. Therefore strips are cut from the wafer (Figure 3.23). These strips are then placed in a chassis made of PTFE (Figure 3.24). The electrical contact is made via three needles, which are previously set to the exact distance between the contact pads. Screws under the aluminum strip are used to move the entire strip up, and thus the stationary needles make electrical contact with the pads. In Figure 3.26 a close-up of a contacted device is shown. The PTFE block with the device is then fixed in the vacuum chamber and the needles are led electrically out of the chamber via a flange.

### 3.6.2 Detecting Resonant Frequencies

All components are measured under high vacuum ( $10^{-4}$  mbar). First, a frequency sweep from 50 kHz to 10 MHz is performed with photo-thermal actuation. The same frequency range is then scanned with actuation via the electrodes (for the individual electrodes as well as for both electrodes together with parallel feeding). As an example, the frequency sweeps for a  $30\ \mu\text{m}$  wide and  $150\ \mu\text{m}$  long poly silicon beam (layer thickness approx.  $4\ \mu\text{m}$ ) are shown in Figure 3.27.

This measurement is only used to find the respective resonance frequencies, for the exact determination of the respective resonance frequency and the amplitude, a separate sweep is carried out around this resonance frequency for each peak that is found (as an

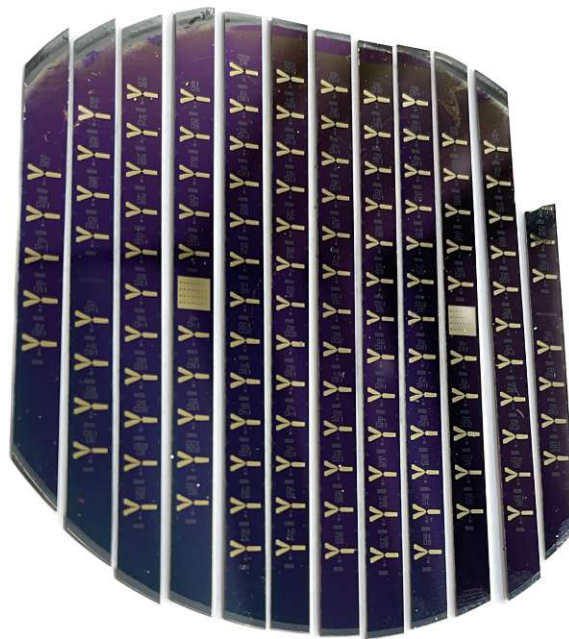


**Figure 3.23:** Optical micrograph of a finished, 4 inch wafer cut into strips.

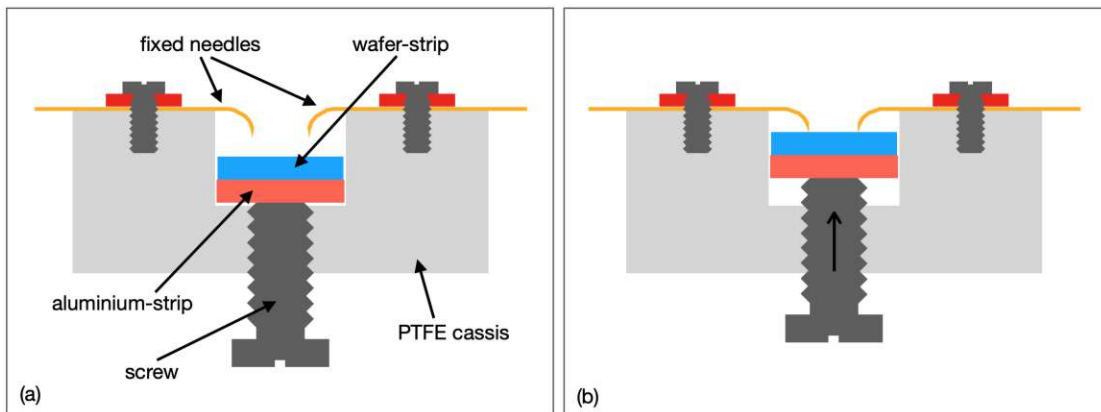


**Figure 3.24:** Schematic illustration how a single device is contacted: the needles are fixed on the chassis and a wafer-strip is placed in a groove on top of an aluminium-strip. By turning the screws under the aluminium-strip, the whole wafer-strip gets elevated until the needles make contact with the device.

example: Figure 3.28 for the 2<sup>nd</sup> Resonance Peak).

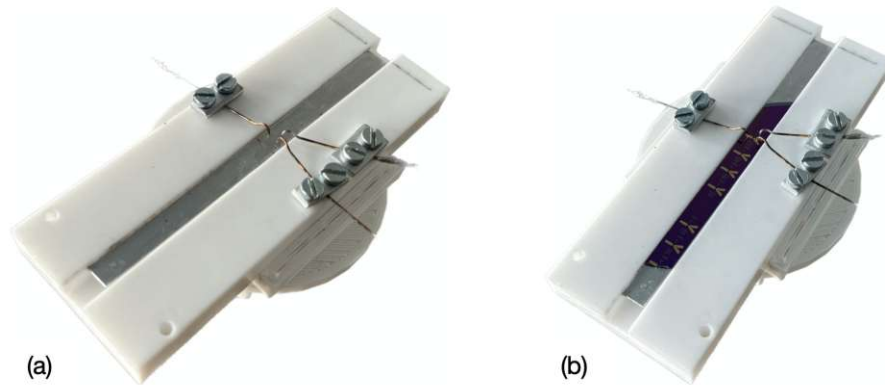


**Figure 3.25:** PTFE Chassis with the three contacting needles: left without a wafer-strip, right with a contacted device



**Figure 3.26:** Close-up of a contacted device: The cantilever is being contacted with the right needle, the two needles on the left are for the big and small electrodes

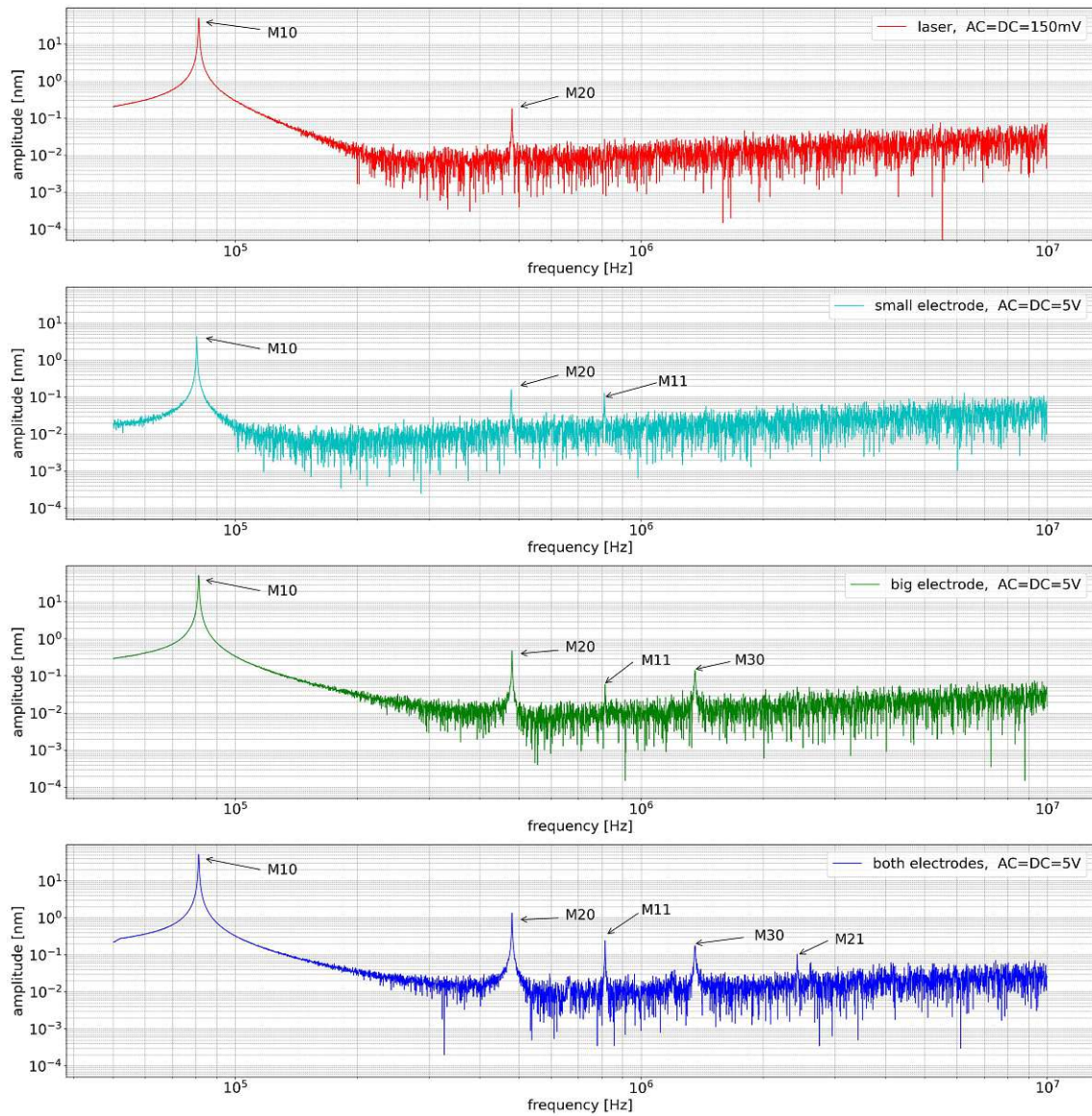


**Figure 3.27:** Examples of measurements with various types of excitation: thermal excitation (red) clearly shows that only the low-frequency modes are measurable. The higher modes are visible using the electrodes, whereas the amplitudes of the mechanical oscillation depends on the selected electrode.

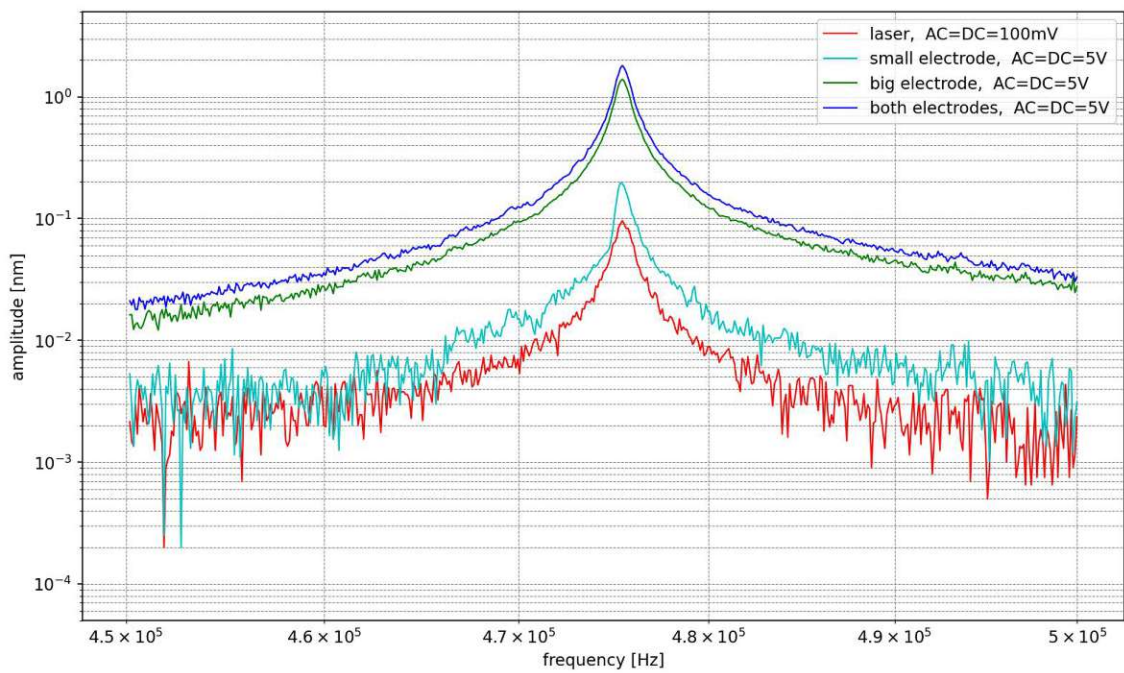


**Figure 3.28:** Examples of a frequency sweep with thermal and electrostatic actuation around the 2<sup>nd</sup> resonance peak (M20)

### 3.6.3 Resonance Fit

To determine an appropriate function for data fitting, a damped harmonic oscillator is assumed with an external sinusoidal force acting upon it.

$$\ddot{x}(t) + \omega_0 Q^{-2} \dot{x}(t) + \omega_0^2 x(t) = \omega_0^2 X_0 \cos(\omega t) \quad (3.1)$$

The resulting deflection of the oscillation can be calculated by

$$x(t) = x_0 \cos(\omega t + \phi). \quad (3.2)$$

By substituting eq. (3.2) into Equation (3.1), a frequency-dependent term for the deflection can be calculated:

$$x(\omega) = \frac{A}{\sqrt{\left(1 - \left(\frac{\omega}{\omega_0}\right)^2\right)^2 + Q^{-2} \left(\frac{\omega}{\omega_0}\right)^2}} \quad (3.3)$$

This function is then utilized in conjunction with the least square method to derive values for the resonance frequency  $\omega_0$  and the  $Q$ -factor from the measured data. Figure 3.29 shows an example of such a fit.

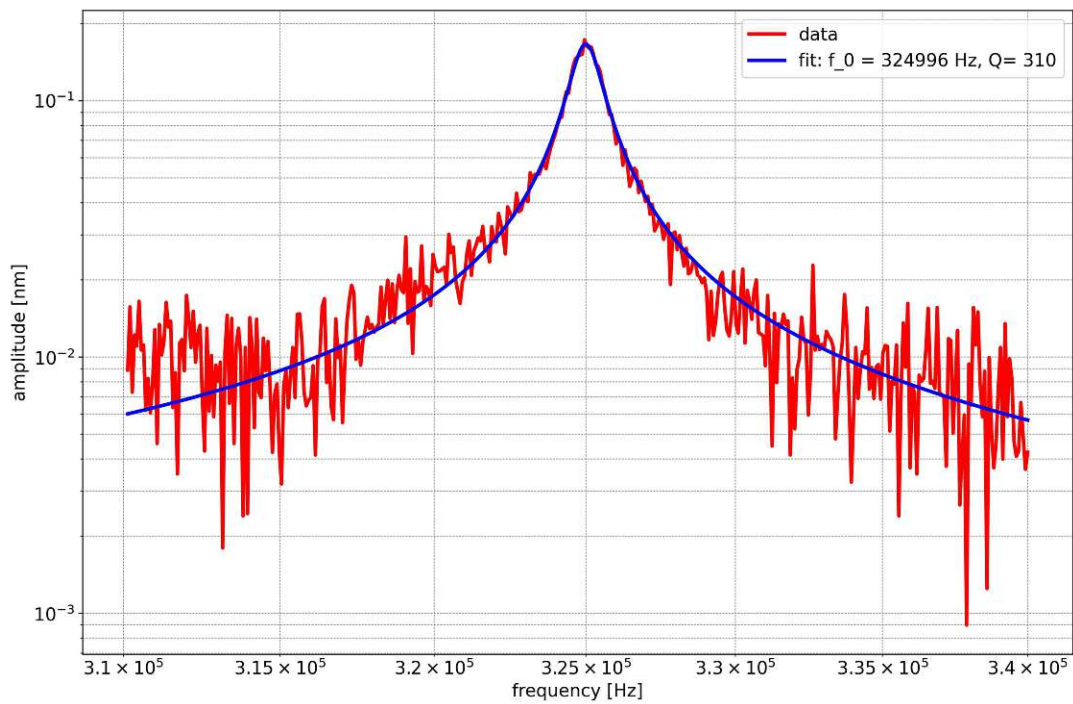


**Figure 3.29:** Example of a noisy measurement fitted with Equation (3.3).

### 3.6.4 Mode Identification

To identify the mode, the previously determined resonance frequency is set as a reference in the lock-in amplifier and the bandpass filter is set to a very narrow bandwidth to minimize noise. Afterwards, the measuring point of the laser-doppler vibrometer is moved slowly over the cantilever (both from the anchor to the front edge and along the front edge). This allowed the observation of the local minima, maxima and the nodal lines. With this information, the respective mode of the resonance frequency is determined.

### 3.7 Circular Transmission Line Measurement

The circular transfer length method (CTML) is used to determine the electrical conductivity of the doped materials. Here, circular structures (Figure 3.30) are deposited on the surface of the wafer, which act as ohmic contacts to the semiconductor material. The basic idea of this method is that a voltage applied between the inner electrode and the outer electrode causes a current to flow through the doped layer. The current depends on the sheet resistance of this doped layer  $R_S$ , the transfer resistance from the metal to the semiconductor  $R_C$  and the effective length of the ohmic contact  $L_T$  (transfer length). Assuming that the radii of the circles are much larger than the transfer length, then the Equation (3.4) is a good approximation. A voltage ramp ranging from -3 V to 3 V is applied to each of the nine different circles in one row on the surface (Figure 3.30 a). The resulting current is logged, allowing  $R_{Tot}$  to be calculated for each of the nine gaps. These resistance values are then fitted with Equation (3.4), whereby the parameters for  $R_S$ ,  $R_C$ ,  $L_T$  are found.

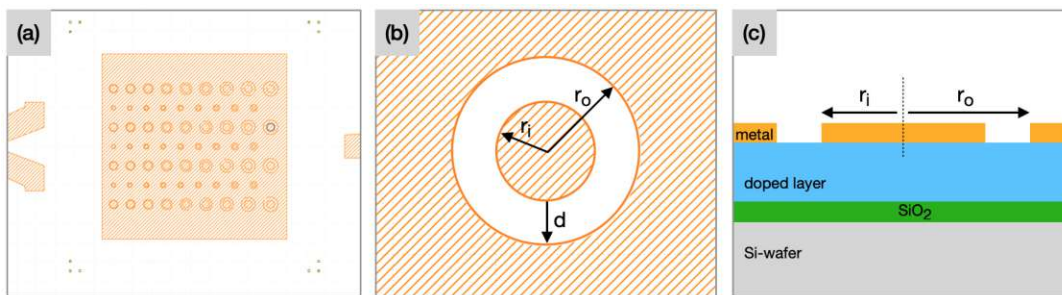


**Figure 3.30:** Dedicated CTLM-area on mask (a), closeup of a single circle (b), cross section on wafer (c)

$$R_{Tot} \approx \frac{R_S}{2\pi i} \left( \ln \frac{r_o}{r_o - d} + L_T \left( \frac{1}{r_o - d} + \frac{1}{r_o} \right) \right) \quad (3.4)$$

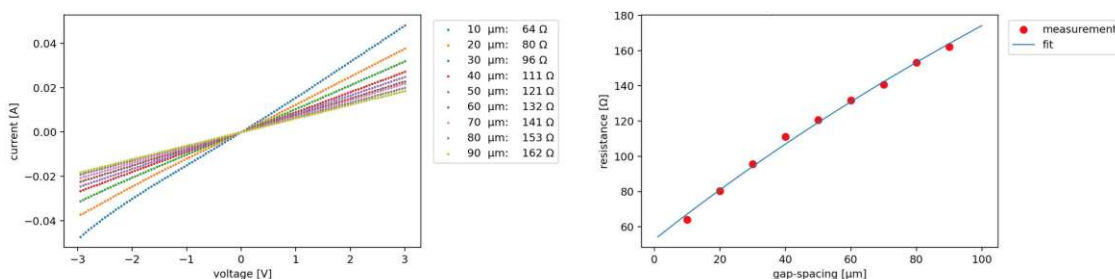


**Figure 3.31:** CTLM measurement and fit example: the nine resistance values (left) and the fitted function to these points (right)

## 3.8 Layer Thickness Measurement

The comb structure (Figure 3.1 and Figure 3.2) can be measured with a profilometer (Bruker DektakXT Surface Profiler) to determine the exact thickness of the cantilever. In Figure 3.32 an example of a measurement of such a comb structure is shown. The metalization layer (100 nm) is applied on top of the polycrystalline layer, which means that the actual thickness of the polycrystalline material is not  $2.23\ \mu\text{m}$ , but  $2.13\ \mu\text{m}$ . This method can offer a very precise estimation of the cantilever's layer thickness by assuming minimal deviation of the polycrystalline layer from the neighboring cantilever to the measuring area.

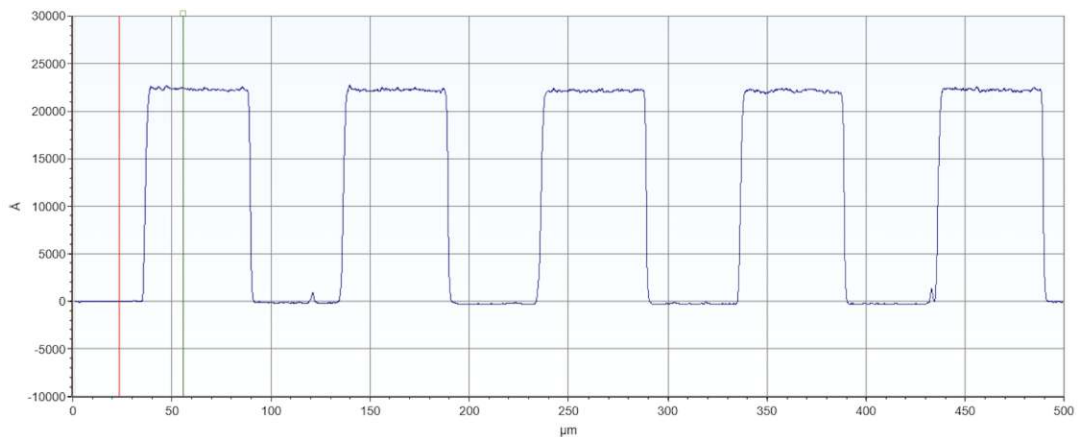


**Figure 3.32:** Example of a measurement of the comb structure next to a Cantilever made out of poly silicone: the height of the device layer including the metal coating totals approx.  $2.23\ \mu\text{m}$ .

Die approbierte gedruckte Originalversion dieser Diplomarbeit ist an der TU Wien Bibliothek verfügbar  
The approved original version of this thesis is available in print at TU Wien Bibliothek.

## 4 Results and Proof of Concept

### 4.1 Linearity of the Electrostatic Actuation

Due to the fact that periodic electrostatic actuation always causes a constant component of the resulting force between the electrodes, the effect of such a constant force on a cantilever is first investigated. For this purpose, M10 of a cantilever (mdiamond, length: 200  $\mu\text{m}$ , width: 30  $\mu\text{m}$ , dual electrode design, both electrodes connected in parallel) is electrostatically actuated. First, the frequency band around the resonance frequency is recorded ten times in a row to determine the statistical distribution of the resonance frequency and the  $Q$ -factor. A DC voltage of 10 V with an AC signal of 20 Vpp (peak-to-peak voltage) is used for the electrostatic actuation. The fit of all these measurements resulted in almost the same resonance frequency with a standard deviation of 0.016%, however the  $Q$ -factor showed a standard deviation of about 1%. Next, the AC voltage is set to 2 Vpp, and the DC voltage is set to different values ranging from 2 V to 20 V. The resonance frequency, the  $Q$ -factor and their standard deviation were again in the same range as in the previous measurement. It can therefore be assumed that the DC component of the electric field does not cause any noticeable change in the resonant frequency and the  $Q$ -factor, in the investigated voltage range.

To determine whether the AC voltage amplitude is in a linear relationship with the deflection, a constant 5 V DC component with different AC voltages is applied. Figure 4.1 shows the fairly linear increase in deflection for M10 according to different AC voltages, therefore it can be said, that for AC voltages up to 10 Vpp the deflection corresponds to the actuation voltage. This linear relationship was also observed for much higher voltages up to 150 V.

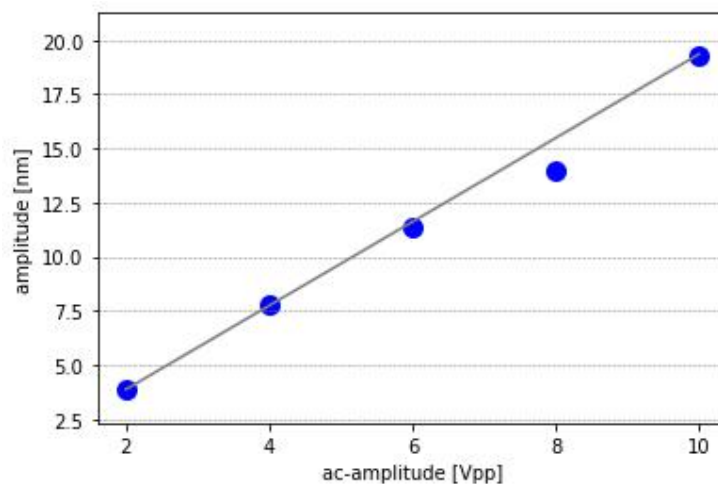


**Figure 4.1:** Electrostatic actuation with 5 V DC-offset and increasing ac-amplitudes at 324.35 kHz (M10). The blue dots mark the deflection at the resonance frequency of the M10 mode at the respective AC amplitude of the drive signal, the gray line represents the linear fit.

## 4.2 Bandwidth Limitation

In principle, the effective capacitance between cantilever and electrode should be in the range of a few femto farads (see chapter simulation). However, the parasitic impedance of the contact pads, the contacting needles, the leads, etc. must also be taken into account. In order to be able to roughly estimate the cut-off frequency of the entire setup, a  $1/4\text{ W}$  metal film resistor with  $50\ \Omega$  is installed in the signal path (Figure 4.2). A frequency sweep is carried out with the lock-in amplifier and the voltage occurring after the  $50\ \Omega$  resistor is measured (Figure 4.3). The cut-off frequency found in this way allows a very rough estimate of the frequency at which the effective low-pass filter of the test setup has attenuated the voltage signal to such an extent that the electric field between the cantilever and the electrode no longer corresponds to the voltage set with the signal generator. This approach is only valid if the parasitic capacitance is several orders of magnitude larger than the capacitance between the electrode and the cantilever and the overall path-resistance to the device under test is much smaller than the  $50\ \Omega$  resistor. In other words, the low-pass of the signal path from the signal generator to the component is already viable at much lower frequencies than the low-pass formed by the cantilever and the electrode. Form this measurement, it can be assumed that signals up to approx. 5 MHz are not yet noticeably attenuated.

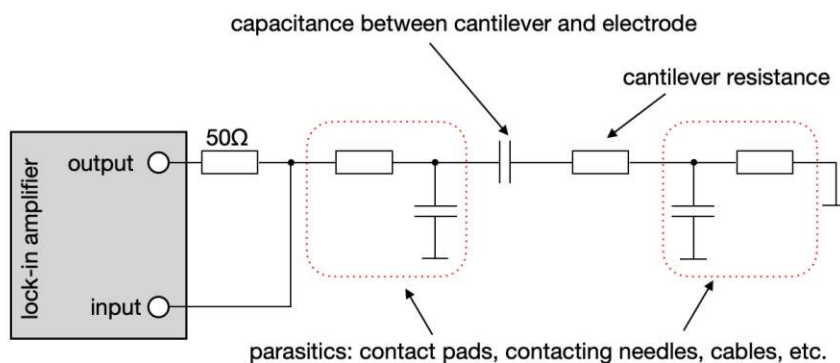


**Figure 4.2:** Equivalent circuit: the two RC low-pass filters are formed by the cables and the contacts with the needles, whereby the resistance is significantly less than the  $50\ \Omega$  measuring resistance. The RC low-pass filter effective for the actuation is determined by the resistance over the cantilever and the capacitance between cantilever and electrode.

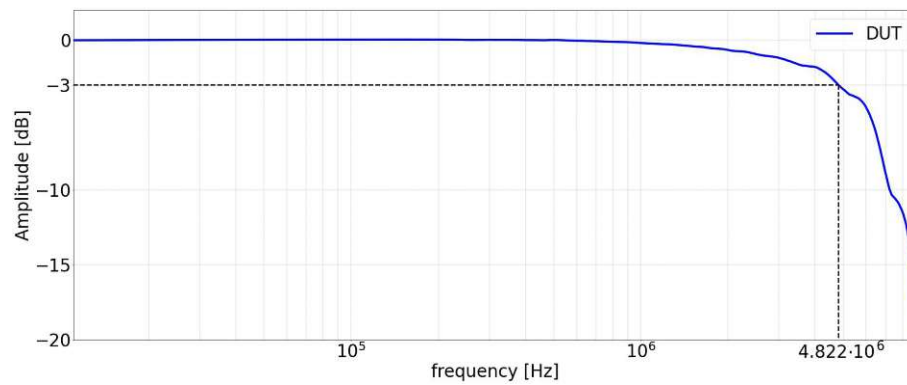


**Figure 4.3:** Signal attenuation with the  $50\ \Omega$  measuring resistor: the  $-3\text{dB}$  cut-off frequency ranges at approx. 5 MHz.

## 4.3 Euler–Bernoulli Beams

### 4.3.1 Single Electrode Design

A cantilever with a length of  $200\ \mu\text{m}$  and a width of  $30\ \mu\text{m}$  is used to verify the general functionality of the single electrode design (Figure 4.4). The device layer of the cantilever is mdiamond with a layer thickness of approx.  $2.2\ \mu\text{m}$ . The frequency sweeps for photo-thermal and electrostatic actuation are shown in Figure 4.5. For photo-thermal actuation, the control voltage is set to a DC offset of 150 mV with a 300 mVpp AC component. In the case of electrostatic actuation, a DC offset of 5 V with an AC voltage of 10 Vpp is applied. The three resonance peaks, which are identified as M10, M20 and M30, are clearly visible with the electrostatic actuation. The cantilever under investigation was modeled using an finite element method (FEM). The geometric dimensions of the cantilever were set equal to those of the mdiamond cantilever. For the Young's modulus and the density, the values were varied until the three modes occurred at the same frequencies as the measurements showed. According to the results of this simulation, the mode M11 should be present at approximately 1.321 MHz (between M20 and M30 in the frequency spectrum). As already described in Section 3.1 and now also

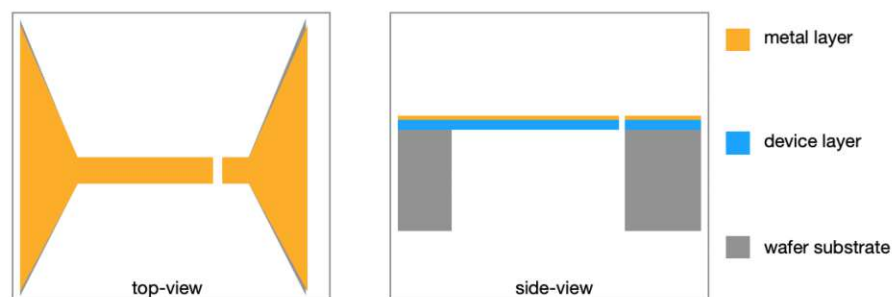


**Figure 4.4:** Schematic of the component: the device layer consists of undoped mdiamond and the metal layer of 20 nm Cr and 80 nm Au

demonstrated experimentally, the torsion mode can not be actuated with this electrode design. In Figure 4.6, the amplitudes of the different modes are compared with the two actuator principles. Both, photo-thermal and electrostatic actuation generate approximately the same amplitude for the M10 mode. However, M20 shows far less amplitude with photo-thermal actuation than with electrostatic actuation. This could result from several effects. First, both M20 and M30 are already above the cut-off frequency of the laser driver, so the signal is already attenuated. In addition, at these frequencies the heat dissipation and heat conduction in the material may already be too slow to follow the waveform of the laser.

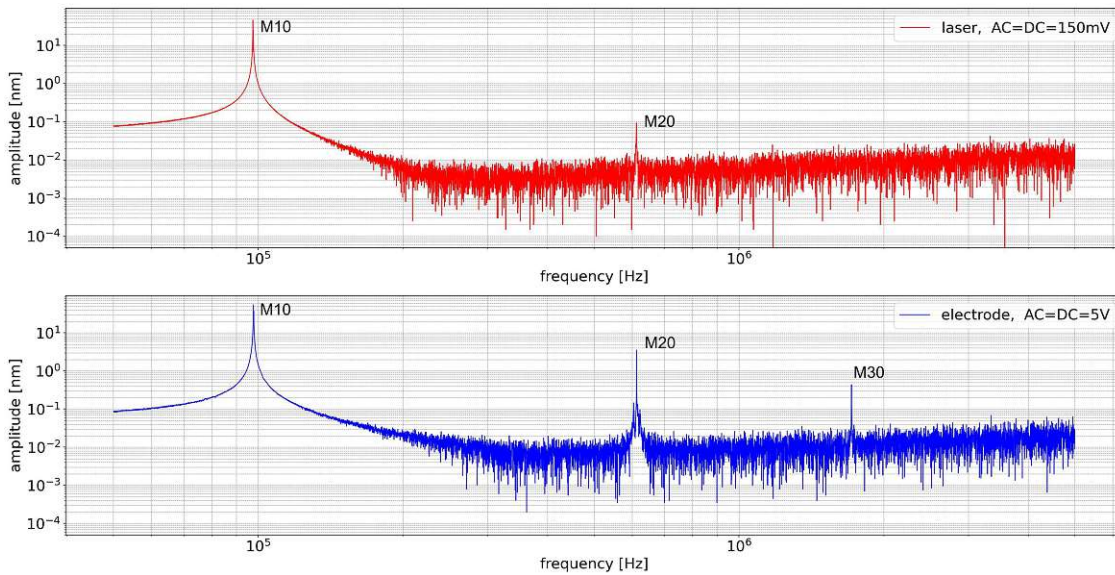


**Figure 4.5:** Frequency sweep of a mdiamond cantilever with both photo-thermal and electrostatic actuation: the 2<sup>nd</sup> resonance peak has a smaller amplitude with photo-thermal actuation, the 3<sup>rd</sup> resonance peaks frequency is over the cutoff frequency of the laser and therefore just visible with electrostatic actuation

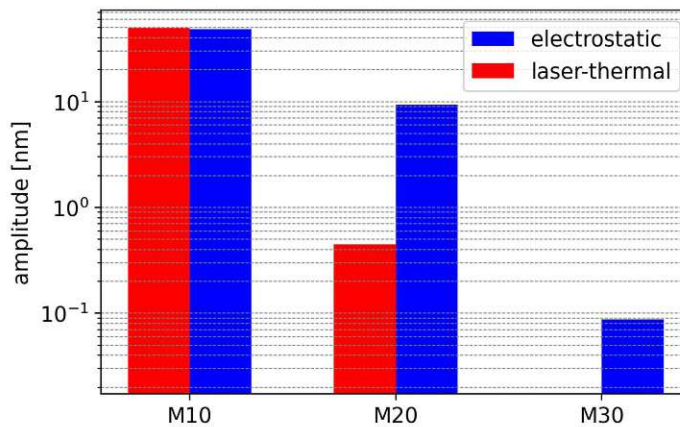


**Figure 4.6:** Comparison of the amplitude of each mode with the respective actuation type

### 4.3.2 Dual Electrode Design

To determine the effectiveness of this design, one doped and one undoped cantilever is measured. In the following subsections, all cantilevers investigated have a length of  $150\ \mu\text{m}$ , a width of  $30\ \mu\text{m}$  and a thickness of around  $3\ \mu\text{m}$ .

#### 4.3.2.1 Undoped Device Layer

For the undoped cantilever, a polySi device-layer is used, with the electrically conductive layer consisting of 20 nm chromium and 80 nm gold (Figure 4.7).

The frequency sweeps (Figure 4.8) show that only the first two modes can be measured with photo-thermal actuation. With electrostatic actuation, three resonances are already recognizable even with the smaller of the two electrodes. A more precise measurement of each mode allows a comparison of the deflection with different electrodes (Figure 4.9). In contrast to the measurement with the single electrode design, M11 can now also be actuated. If the two electrodes are connected in parallel, they behave quite similar to a large electrode located opposite the cantilever. For the torsion mode, this means much lower deflection, as the electrostatic force acts in phase on both sides of the cantilever, and therefore very little energy is transferred to this resonance, resulting in an inefficient excitation scheme. The same applies to a lower extent to M21, where the connection of the electrodes also results in a lower deflection than with the large electrode alone. The opposite is observed for M10, M20 and M30, where connecting the electrodes results in a larger deflection than with each electrode alone. This behavior is also to be expected, as the front edge oscillates in phase with the signal and thus the connected electrodes can generate more force.

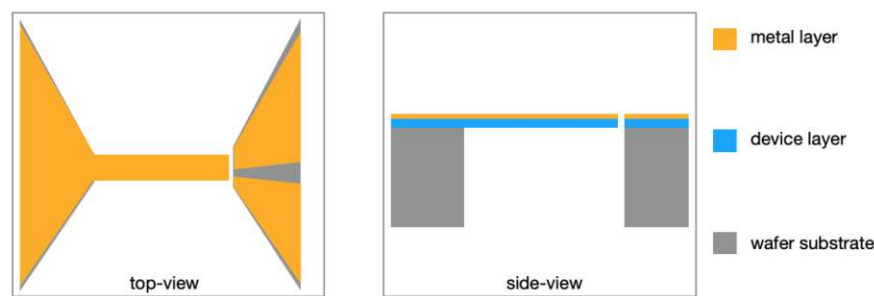


**Figure 4.7:** Schematic of the component: the device layer consists of undoped polySi and the metal layer of 20 nm Cr and 80 nm Au

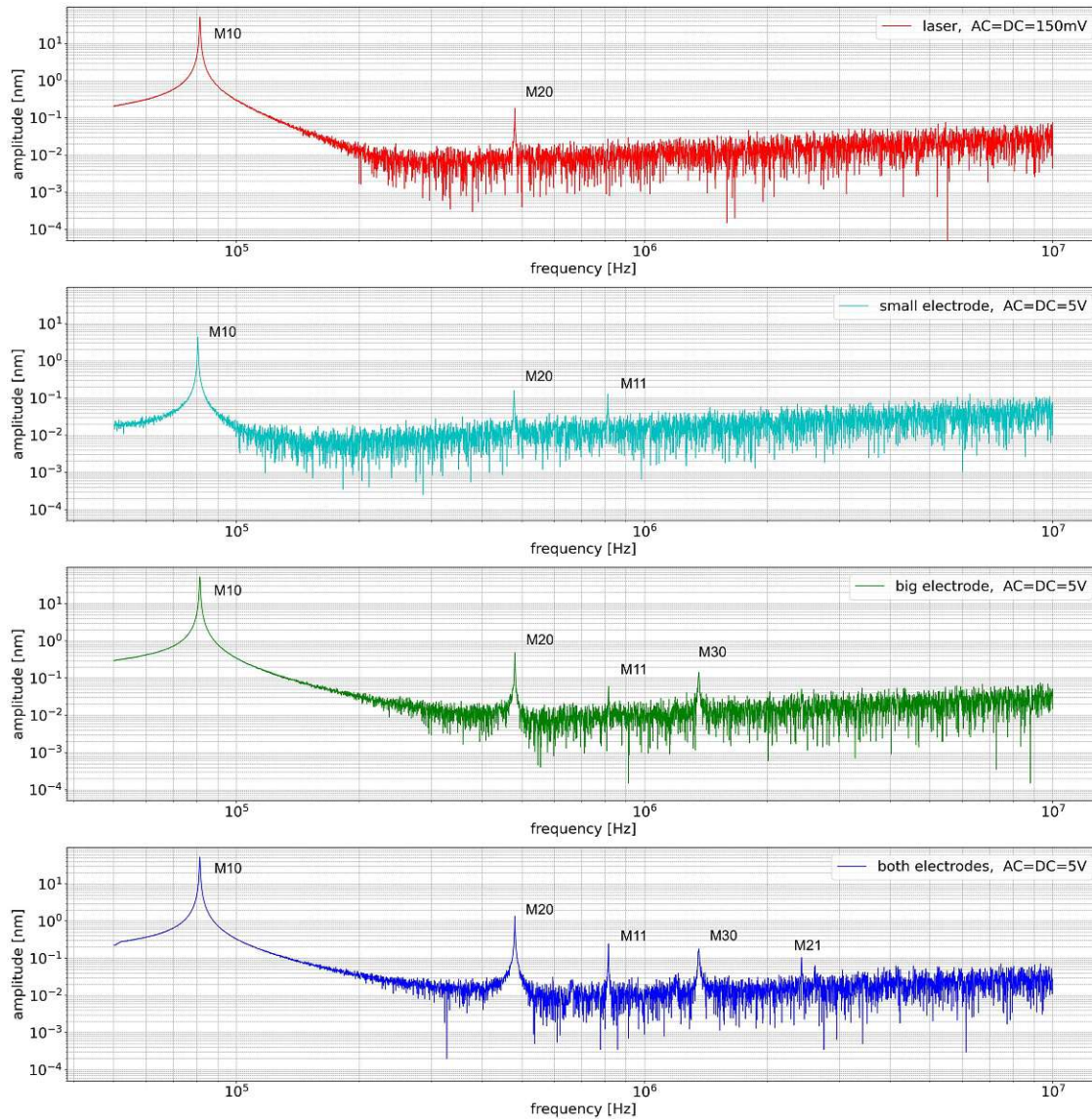


**Figure 4.8:** Frequency sweeps of a polySi cantilever: the photo-thermal actuation works only for the first two modes (red), the higher frequency modes are visible with electrostatic actuation

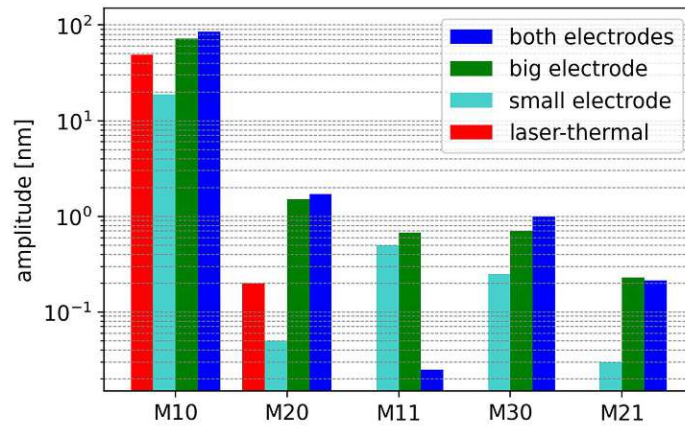


**Figure 4.9:** PolySi cantilever: comparison of the amplitude of each mode with the respective actuation type

## 4.3.2.2 Doped Device Layer

The material of the cantilever is boron doped ndiamond, with the contact material consisting of 20 nm titanium and 80 nm gold (Figure 4.10). Three modes can be identified when electrostatically actuated (Figure 4.11). The amplitudes of the modes are again measured exactly at the resonance frequency in order to compare the photo-thermal actuation with different electrode configurations (Figure 4.12). Interestingly, the amplitude of M10 with actuation from the small electrode was larger than with the large electrode. This effect is not seen with M20, where less amplitude is achieved when the two electrodes are connected, compared to actuation with the large electrode. One possible explanation could be the irregularities of the polycrystalline material. In some modes it was noticed that the deflection was not symmetrical, for example that one corner had a higher deflection than the other. This behavior would indicate that the material does not behave homogeneously and therefore an asymmetrical mode occurs.

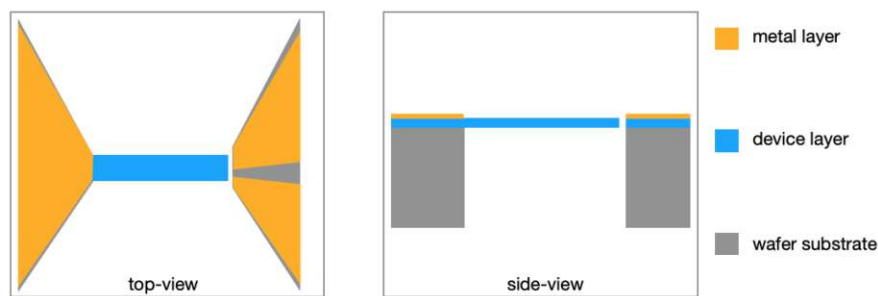


**Figure 4.10:** Schematic of the component: the device layer consists of doped ndiamond and the metal layer of 20 nm Ti and 80 nm Au

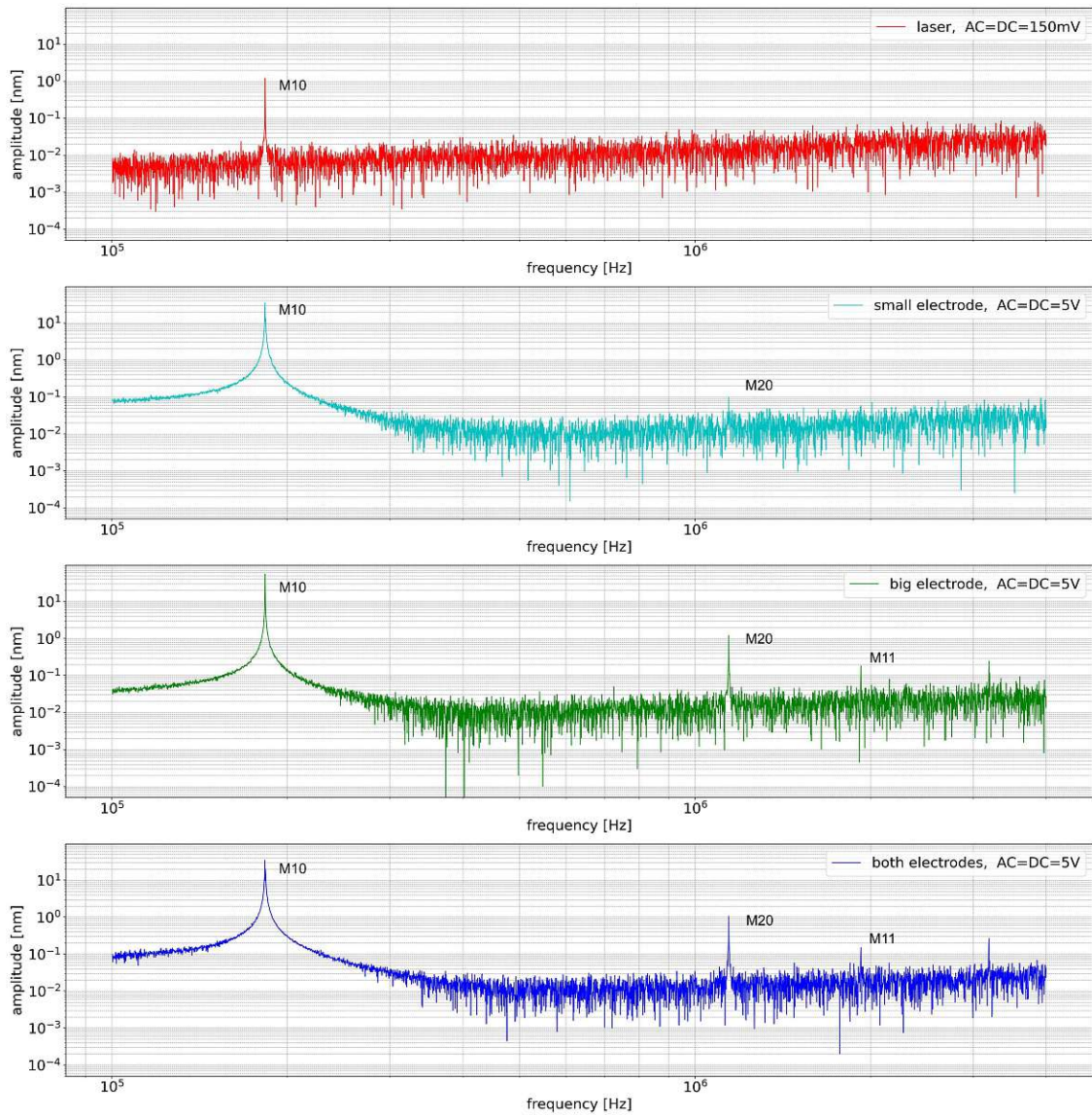


Figure 4.11: Frequency sweeps of a doped ndiamond cantilever

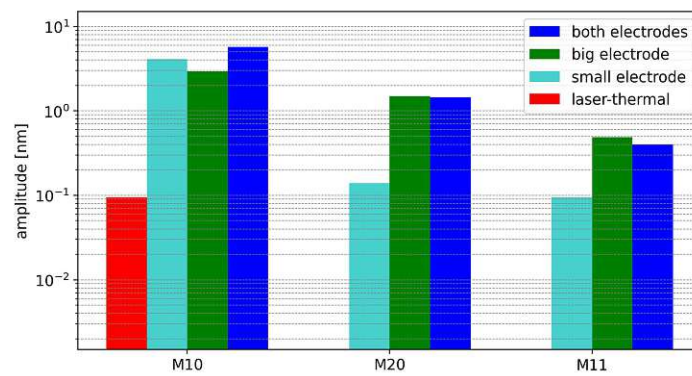
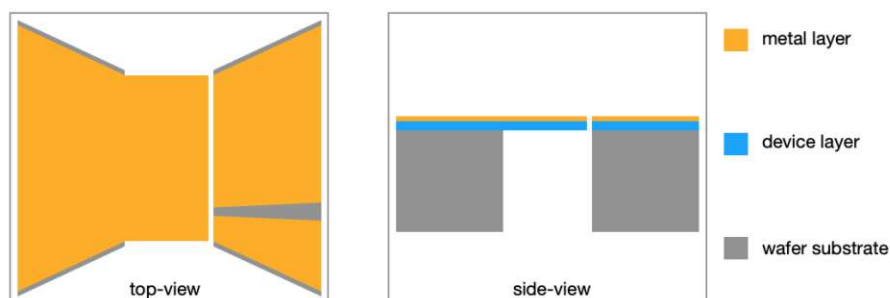


Figure 4.12: Doped ndiamond cantilever: comparison of the amplitude of each mode with the respective actuation type

## 4.4 Plate Resonators

The ability to actuate wide, single-side clamped plates is discussed in this section. The investigated cantilever is fabricated from undoped polySi, with a width of  $200\ \mu\text{m}$  and a length of  $100\ \mu\text{m}$  (Figure 4.13). For the metal coating, 20 nm titanium with 80 nm gold on top is used. With photo-thermal actuation, it can be seen that only the first two modes can be measured (Figure 4.14 and Figure 4.15). The low displacement in relation to the electrostatic excitation is probably due to the fact that the laser always introduces the same amount of energy into the material, regardless of the size of the resonator. However, as the electrodes get bigger as the resonator gets bigger, more force is generated to actuate the structure. With electrostatic actuation, depending on the electrodes used, up to seven modes can be actuated. The roof-tile shaped mode M13 is supposed to be in the measured frequency range, nevertheless, due to effects in the resonator, e.g. cross talk between modes, its response is distorted and not further investigated.

For M10, the deflection is largest when both electrodes are connected in parallel, which is to be expected as the effective electrode area is also largest here. Interestingly, M11 does not behave as expected, as here the two corners don't oscillate in phase and connecting the electrodes together should decrease the deflection. Even with the higher modes, the relationship between deflection and electrode configuration is not always as expected. For example, as with M10, M20 should have the largest deflection when both electrodes are driven in parallel, but this is not the case. This behavior could again be due to inhomogeneities in the device layer.



**Figure 4.13:** Schematic of the component: the device layer consists of undoped polySi and the metal layer of 20 nm Ti and 80 nm Au

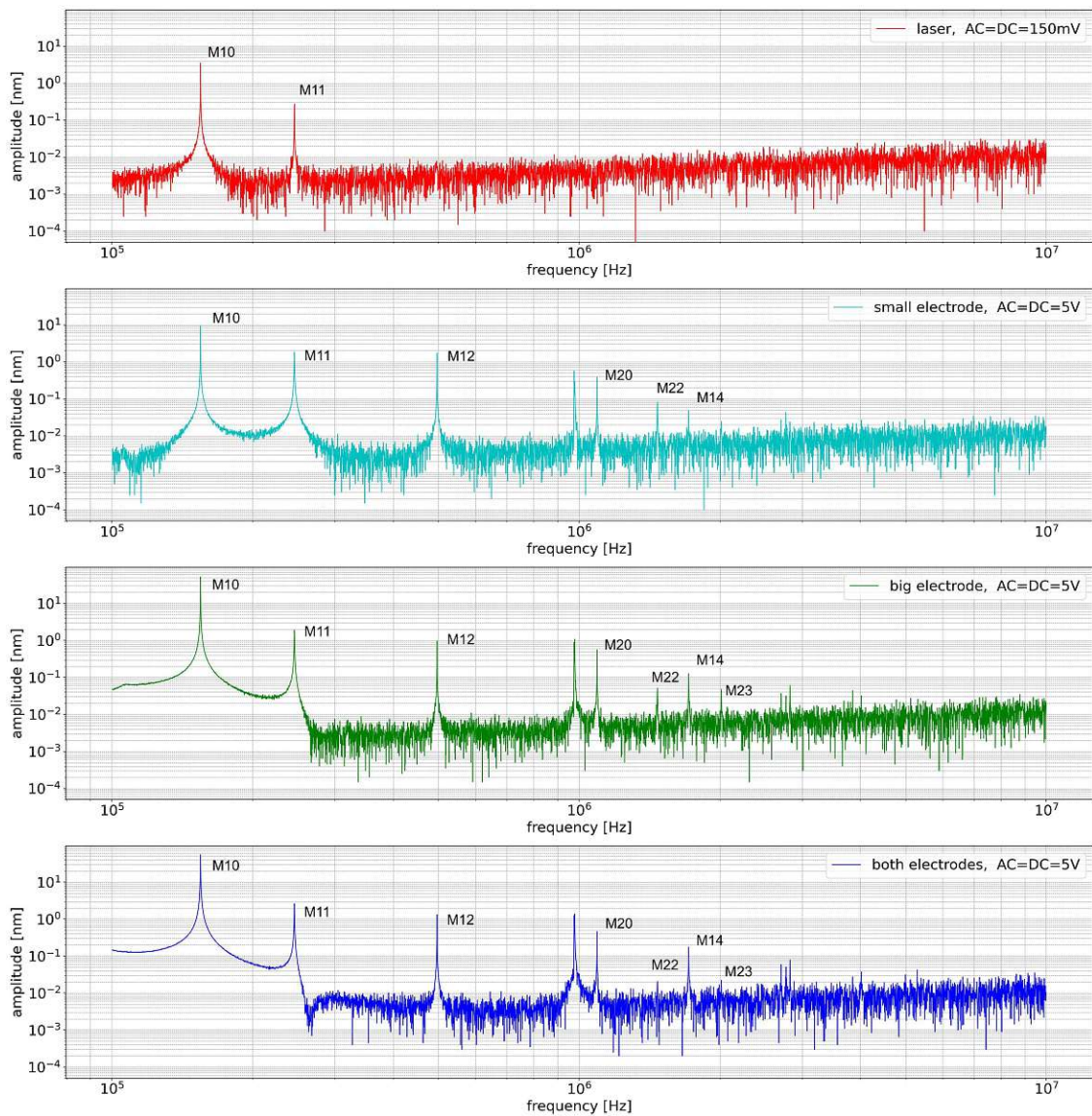
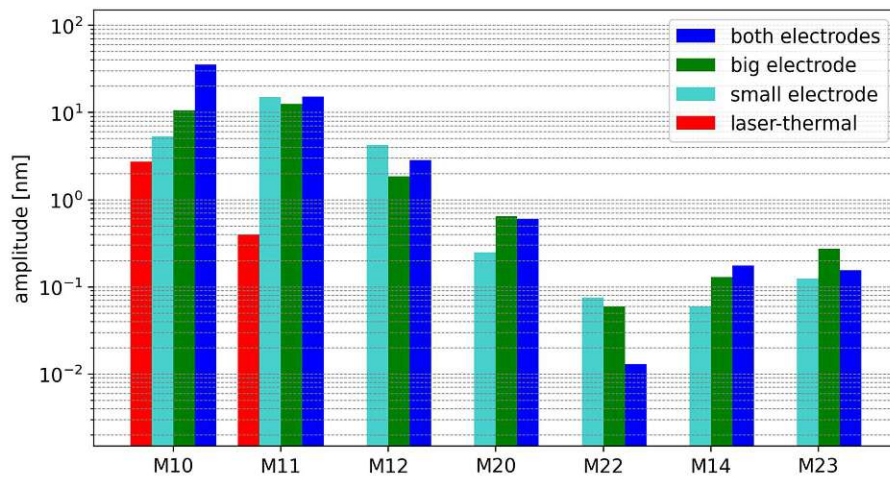


Figure 4.14: Frequency sweeps of a polySi plate-like resonator



**Figure 4.15:** PolySi resonator: comparison of the amplitude of each mode with the respective actuation type

## 5 Conclusions and outlook

This work introduced a basic resonator design that allows for the utilization of doped and undoped polycrystalline thin films to fabricate resonators, excited by electrostatic actuation. The actuation principle was compared to photo-thermal actuation on both wide plate resonators and narrow Euler-Bernoulli cantilevers. The high actuating capability, especially for higher out-of-plane modes, was demonstrated for various doped and undoped polycrystalline materials. It was also shown that the actuation method does not result in a measurable change in the resonance frequency and the  $Q$ -factor. The need for a more thorough investigation arises from the occasional, unpredicted variations in deflection observed across diverse electrode configurations.

In comparison to laser-thermal actuation, this method achieved higher deflections and frequencies in the investigated frequency range. Limitations imposed by the parasitic effects of the measurement setup restricted measurements to 5 MHz. Utilizing metal wire bonding for contacts and shortening the cable lengths could enable measurements at higher frequencies. Also, increasing the drive voltage can enable measurements up to higher frequencies.

One possible application for this type of transducer is as a test structure in order to obtain information about the local material parameters arising from the resonance frequencies and the  $Q$ -factor. Another feasible use are MEMS oscillators, whereby the electrical readout of the oscillation would have to be investigated, which was not in the focus of this work. Nevertheless, thanks to the small capacitance, resonances at very high frequencies can be actuated, which is particularly interesting for precise clock generators.

Die approbierte gedruckte Originalversion dieser Diplomarbeit ist an der TU Wien Bibliothek verfügbar  
The approved original version of this thesis is available in print at TU Wien Bibliothek.



# Bibliography

- [1] H. C. Nathanson, W. E. Newell, R. A. Wickstrom, and J. R. Davis, "The resonant gate transistor," *IEEE Transactions on Electron Devices*, vol. 14, no. 3, pp. 117–133, 1967.
- [2] L.-S. Fan, Y.-C. Tai, and R. Muller, "Pin joints, gears, springs, cranks, and other novel micromechanical structures," tech. rep., California Univ., Berkeley (USA), 1987.
- [3] M. J. Madou, *Fundamentals of microfabrication: the science of miniaturization*. CRC press, 2002.
- [4] G. Zhanshe, C. Fucheng, L. Boyu, C. Le, L. Chao, and S. Ke, "Research development of silicon mems gyroscopes: A review," *Microsystem Technologies*, vol. 21, pp. 2053–2066, 2015.
- [5] O. Brand, O. Brand, I. Dufour, S. Heinrich, and F. Josse, *Resonant MEMS: fundamentals, implementation, and application (Advanced micro and nanosystems)*, vol. 11 of *Advanced Micro and Nanosystems*. Newark: WILEY, 1 ed., 2015.
- [6] J. Van Beek and R. Puers, "A review of mems oscillators for frequency reference and timing applications," *Journal of Micromechanics and Microengineering*, vol. 22, no. 1, p. 013001, 2011.
- [7] K. Y. Yasumura, T. D. Stowe, E. M. Chow, T. Pfafman, T. W. Kenny, B. C. Stipe, and D. Rugar, *Quality Factors in Micron- and Submicron-Thick Cantilevers*, vol. 9. 2000.
- [8] A. S. Algamili, M. H. M. Khir, J. O. Dennis, A. Y. Ahmed, S. S. Alabsi, S. S. Ba Hashwan, and M. M. Junaid, "A review of actuation and sensing mechanisms in mems-based sensor devices," *Nanoscale research letters*, vol. 16, pp. 1–21, 2021.
- [9] P. Di Barba, T. Gotszalk, W. Majstrzyk, M. E. Mognaschi, K. Orłowska, S. Wiak, and A. Sierakowski, "Optimal design of electromagnetically actuated mems cantilevers," *Sensors*, vol. 18, no. 8, p. 2533, 2018.
- [10] M. Kucera, E. Wistrela, G. Pfusterschmied, V. Ruiz-Díez, T. Manzanque, J. Hernando-García, J. L. Sánchez-Rojas, A. Jachimowicz, J. Schalko, A. Bittner, *et al.*, "Design-dependent performance of self-actuated and self-sensing piezoelectric-aln cantilevers in liquid media oscillating in the fundamental in-plane bending mode," *Sensors and Actuators B: Chemical*, vol. 200, pp. 235–244, 2014.
- [11] C.-H. Chu, W.-P. Shih, S.-Y. Chung, H.-C. Tsai, T.-K. Shing, and P.-Z. Chang, "A low actuation voltage electrostatic actuator for rf mems switch applications," *Journal of micromechanics and microengineering*, vol. 17, no. 8, p. 1649, 2007.
- [12] R. Maboudian, "Surface processes in mems technology," *Surface Science Reports*, vol. 30, no. 6-8, pp. 207–269, 1998.
- [13] M. A. Rosa, D. De Bruyker, A. R. Völkel, E. Peeters, and J. Dunec, "A novel external electrode configuration for the electrostatic actuation of mems based devices," *Journal of Micromechanics and Microengineering*, vol. 14, no. 4, p. 446, 2004.
- [14] Polytec, "Basic measurement principle of vibrometry and setup of a laser doppler vibrometer."
- [15] F. Klauser, D. Steinmüller-Nethl, R. Kaindl, E. Bertel, and N. Memmel, "Raman studies of nano- and ultra-nanocrystalline diamond films grown by hot-filament cvd," *Chemical Vapor Deposition*, vol. 16, no. 4-6, pp. 127–135, 2010.
- [16] T. Yamada, H. Yoshikawa, H. Uetsuka, S. Kumaragurubaran, N. Tokuda, and S.-i. Shikata, "Cycle of two-step etching process using icp for diamond mems applications," *Diamond and related materials*, vol. 16, no. 4-7, pp. 996–999, 2007.



## List of Figures

2.1	Two dimensional model of a single side clamped cantilever, also called <i>Euler-Bernoulli beam</i> . . . . .	3
2.2	First three mode shapes of the simple Euler-Bernoulli cantilever . . . . .	4
2.3	The first four mode shapes of a thin single-side clamped cantilever with a length to width ratio of 20:3. The color gradient shows the deflection, with green indicating no deflection and red the largest deflection. . . . .	5
2.4	A few examples of mode shapes of a thin plate clamped on one side with a length to width ratio of 1:2. . . . .	5
2.5	The mode shapes are labeled by enumerating the nodal lines as illustrated	5
2.6	Mechanical model of a damped harmonic oscillator with external excitation. The mass $m$ is connected to a spring $k$ and a damper $d$ on a rigid surface, with an external force $F_{ext}$ acting on the mass. . . . .	6
2.7	Amplitude gain and phase of the harmonic oscillator with different values for $\zeta$ . . . . .	7
2.8	Bode plot of the first three resonances of a arbitrary resonator . . . . .	8
2.9	Bode plot of the sum of the first three resonances of an arbitrary resonator as depicted in Figure 2.8 . . . . .	8
2.10	Deflection of various points on a cantilever: Point $\alpha$ is located on the node of the second mode, at $\beta$ the maximum deflection occurs for both mode shapes. The amplitude responses on the right-hand side show the deflection of the beam measured at the different actuation and measurement points. . . . .	9
2.11	Examples of thermal actuation: free beam clamped on both sides (a), a heating element which is surrounded by different materials (bi-material actuator) (b), a laser causes localized heating of a cantilever, resulting in its deflection (c) . . . . .	10
2.12	Electromagnetic actuation of a cantilever: by applying current to the conductor (red path), the external magnetic field (B) causes the cantilever (blue) to bend ( $F_L$ ). A quite similar device was fabricated in [9]. . . . .	11
2.13	Structure of a piezoelectric material: without an external force, the charge centers are in the same position; if an external force is applied, the charge centers separate and an electric field is created . . . . .	12
2.14	The two plates of a capacitor are pulled towards each other by the electrostatic force if a voltage is applied. . . . .	12
2.15	When the two plates are offset, the electrostatic force acts in the direction of this offset. . . . .	13
2.16	Pull-in effect: The position of one electrode can be changed via the electrostatic force if one electrode of the capacitor is attached to a spring. However, if this exceeds a critical point, the spring can no longer counteract and the plates collide. . . . .	13

2.17	Model of a MEMS relay: if a sufficiently high voltage is applied between the metal layer on the cantilever and the electrode underneath, the switch at the front makes contact. The wiring to the electrodes and to the contacts of the switch are not illustrated. . . . .	14
2.18	Separate fabrication of the cantilever and the electrode eliminates the need for wet etching. However, joining the two parts together requires a high degree of precision. . . . .	15
2.19	Electrodes situated to the sides of a Cantilever are easy to fabricate and have the advantage of avoiding pull-in effects. . . . .	15
2.20	Design approach employed for this work: Electrode and resonator are fabricated in one plane (left), after etching a hole from the backside, the resonator experience a stress induced bend, and therefor out-of-plane modes can be electrostatically actuated (right). . . . .	16
3.1	Single electrode design: (a) complete mask overview, (b) single component with $200\mu\text{m}$ overhang, (c) magnification of the same cantilever . . .	17
3.2	Dual electrode Design: (a) complete mask overview, (b) single device with $200\mu\text{m}$ width and $100\mu\text{m}$ overhang, (c) magnification of the same cantilever . . . . .	18
3.3	Basic principle of a profilometer: the cantilever (black) with the diamond tip (blue) is moved over the sample (gray) while the force ( $F_c$ ) on the sample is kept constant. . . . .	19
3.4	Functional principle of a laser-doppler vibrometer [14] . . . . .	20
3.5	Simplified representation showing the signal path of a lock-in amplifier: The noisy signal to be measured is amplified and bandpass filtered around the frequency set on the local oscillator. By multiplying the filtered input signal with the phase-shifted oscillator sinusoidal signal, a DC loaded signal is generated. After lowpass filtering, the DC component remains, the amplitude of which corresponds to the amplitude of the input signal hidden in the noise at the oscillator frequency. . . . .	21
3.6	Laser controller: the temperature of the laser diode is kept constant at $25^\circ\text{C}$ while the laser current is controlled with an external voltage signal.	22
3.7	SEM image of the polySi surface topography. . . . .	23
3.8	Difference between the grain sizes of mdiamond and ndiamond . . . . .	23
3.9	Mask exposure: The mask blocks the ultraviolet light in certain areas. The exposed areas behave differently for negative or positive resists. . .	25
3.10	Simplified illustration of a thermal evaporation plant . . . . .	26
3.11	After depositing the metal layer (a), the photoresist is dissolved with acetone and the aid of ultrasonic waves (b). After complete dissolution of the photoresist (c), the wafer structured with metal remains (d). . . .	26
3.12	System overview of an RIE plant . . . . .	27
3.13	basic operating principle of deep reactive ion etching (Bosch-process) . .	28
3.14	Fabrication steps for undoped polycrystalline diamond . . . . .	29
3.15	Fabrication steps for doped polycrystalline diamond . . . . .	30

3.16	Summary showing the process steps for fabricating the different device layer materials . . . . .	31
3.17	SEM images of the same mdiamond cantilever (200 $\mu\text{m}$ long, 30 $\mu\text{m}$ wide) with a single electrode . . . . .	32
3.18	SEM images of fabricated plate resonators with two electrodes: undoped polySi (a) and doped monocrystalline silicone (b) . . . . .	32
3.19	System setup for the deflection measurement with thermal actuation . . .	33
3.20	System setup for the deflection measurement with electrostatic actuation	33
3.21	Signal to drive the cantilever: An ac sine wave is combined with an equal dc component, the resulting signal has a minimum amplitude of 0 V and a maximum amplitude of double the ac-peak amplitude. . . . .	34
3.22	Position of the thermal actuation laser spot near the anchor and the measurement-laser near the right corner . . . . .	35
3.23	Optical micrograph of a finished, 4 inch wafer cut into strips. . . . .	36
3.24	Schematic illustration how a single device is contacted: the needles are fixed on the chassis and a wafer-strip is placed in a groove on top of an aluminium-strip. By turning the screws under the aluminium-strip, the whole wafer-strip gets elevated until the needles make contact with the device. . . . .	36
3.25	PTFE Chassis with the three contacting needles: left without a wafer-strip, right with a contacted device . . . . .	37
3.26	Close-up of a contacted device: The cantilever is being contacted with the right needle, the two needles on the left are for the big and small electrodes . . . . .	37
3.27	Examples of measurements with various types of excitation: thermal excitation (red) clearly shows that only the low-frequency modes are measurable. The higher modes are visible using the electrodes, whereas the amplitudes of the mechanical oscillation depends on the selected electrode. . . . .	38
3.28	Examples of a frequency sweep with thermal and electrostatic actuation around the 2 <sup>nd</sup> resonance peak (M20) . . . . .	39
3.29	Example of a noisy measurement fitted with Equation (3.3). . . . .	41
3.30	Dedicated CTLM-area on mask (a), closeup of a single circle (b), cross section on wafer (c) . . . . .	42
3.31	CTLM measurement and fit example: the nine resistance values (left) and the fitted function to these points (right) . . . . .	42
3.32	Example of a measurement of the comb structure next to a Cantilever made out of poly silicone: the height of the device layer including the metal coating totals approx. 2.23 $\mu\text{m}$ . . . . .	43
4.1	Electrostatic actuation with 5 V DC-offset and increasing ac-amplitudes at 324.35 kHz (M10). The blue dots mark the deflection at the resonance frequency of the M10 mode at the respective AC amplitude of the drive signal, the gray line represents the linear fit. . . . .	45

4.2	Equivalent circuit: the two RC low-pass filters are formed by the cables and the contacts with the needles, whereby the resistance is significantly less than the $50\ \Omega$ measuring resistance. The RC low-pass filter effective for the actuation is determined by the resistance over the cantilever and the capacitance between cantilever and electrode. . . . .	46
4.3	Signal attenuation with the $50\ \Omega$ measuring resistor: the -3dB cut-off frequency ranges at approx. 5 MHz. . . . .	47
4.4	Schematic of the component: the device layer consists of undoped mdiamond and the metal layer of 20 nm Cr and 80 nm Au . . . . .	47
4.5	Frequency sweep of a mdiamond cantilever with both photo-thermal and electrostatic actuation: the 2 <sup>nd</sup> resonance peak has a smaller amplitude with photo-thermal actuation, the 3 <sup>rd</sup> resonance peaks frequency is over the cutoff frequency of the laser and therefore just visible with electrostatic actuation . . . . .	48
4.6	Comparison of the amplitude of each mode with the respective actuation type . . . . .	48
4.7	Schematic of the component: the device layer consists of undoped polySi and the metal layer of 20 nm Cr and 80 nm Au . . . . .	49
4.8	Frequency sweeps of a polySi cantilever: the photo-thermal actuation works only for the first two modes (red), the higher frequency modes are visible with electrostatic actuation . . . . .	50
4.9	PolySi cantilever: comparison of the amplitude of each mode with the respective actuation type . . . . .	51
4.10	Schematic of the component: the device layer consists of doped ndiamond and the metal layer of 20 nm Ti and 80 nm Au . . . . .	52
4.11	Frequency sweeps of a doped ndiamond cantilever . . . . .	53
4.12	Doped ndiamond cantilever: comparison of the amplitude of each mode with the respective actuation type . . . . .	53
4.13	Schematic of the component: the device layer consists of undoped polySi and the metal layer of 20 nm Ti and 80 nm Au . . . . .	54
4.14	Frequency sweeps of a polySi plate-like resonator . . . . .	55
4.15	PolySi resonator: comparison of the amplitude of each mode with the respective actuation type . . . . .	56